PLEASE CITE THIS ARTICLE AS DOI: 10.1063/5.0146168

### E-H Transitions in Ar/O<sub>2</sub> and Ar/Cl<sub>2</sub> Inductively Coupled Plasmas: Antenna Geometry and Operating Conditions

Tugba Piskin<sup>1</sup>, Yuchen Qian<sup>2</sup>, Patrick Pribyl<sup>2</sup>, Walter Gekelman<sup>2</sup> and Mark J. Kushner<sup>1,3</sup>

- Electrical Engineering and Computer Science Department, University of Michigan, 1301 Beal Ave., Ann Arbor, MI 48109-2122 USA
- Physics Department, University of California, Los Angeles, CA 90095 USA
- <sup>3</sup> Author to whom correspondence should be addressed.

e-mail: <u>tugbap@umich.edu</u>, <u>qianyuchen@ucla.edu</u>, <u>pribyl@ucla.edu</u>, <u>gekelman@physics.ucla.edu</u>, mjkush@umich.edu

### **Abstract:**

Electronegative inductively coupled plasmas (ICPs) are used for conductor etching in the microelectronics industry for semiconductor fabrication. Pulsing of the antenna power and bias voltages provides additional control for optimizing plasma-surface interactions. However, pulsed ICPs are susceptible to capacitive-to-inductive mode transitions at the onset of the power pulse due to there being low electron densities at the end of the prior afterglow. The capacitive (E) to inductive (H) mode transition is sensitive to the spatial configuration of the plasma at the end of the prior afterglow, circuit (matchbox) settings, operating conditions, and reactor configurations, including antenna geometry. In this paper, we discuss results from a computational investigation of E-H transitions in pulsed ICPs sustained in Ar/Cl<sub>2</sub> and Ar/O<sub>2</sub> gas mixtures while varying operating conditions, including gas mixture, pulse repetition frequency, duty cycle of the power pulse, and antenna geometry. Pulsed ICPs sustained in Ar/Cl<sub>2</sub> mixtures are prone to significant E-H transitions due to thermal dissociative attachment reactions with Cl<sub>2</sub> during the afterglow which reduce pre-pulse electron densities. These abrupt E-H transitions launch electrostatic waves from the formation of a sheath at the boundaries of the plasma and under the antenna in particular. The smoother E-H transitions observed for Ar/O<sub>2</sub> mixture results from the higher electron density at the start of the power pulse due to the lack of thermal electron attaching reactions to O<sub>2</sub>. Ion energy and angular distributions (IEADs) incident onto the wafer and the dielectric window under the antenna are discussed. The shape of the antenna influences the severity of the E-H transition and the IEADs, with antennas having larger surface areas facing the plasma producing larger capacitive coupling. Validation of the model is performed by comparison of computed electron densities with experimental measurements.

PLEASE CITE THIS ARTICLE AS DOI: 10.1063/5.0146168

### I. Introduction

The use of plasmas, and inductively coupled plasmas (ICPs) in particular, for etching, passivation, cleaning, and deposition for microelectronics fabrication, and advance processes such as atomic layer etching, is increasing as feature sizes become smaller [1]. The ability to control ion energies and uniformity of reactive fluxes to wafers is important in all aspects of high-volume manufacturing (HVM) [2]. The stability and repeatability of plasma processes are critical to maintaining high yields of the resulting devices [3–6]. Since fine-tuning reactive fluxes to wafers is challenging, multiple parameters are often adjusted, such as flow rate, pressure, power, chamber and antenna geometry, bias voltages on the substrate, and gas composition. Pulsing the power and bias voltages is another strategy to enable additional control of reactive fluxes onto the wafer [7,8]. However, pulsed electronegative ICPs are prone to well-observed phenomena known as E-H (capacitive to inductive) mode transitions [9–14]

The typical ICPs used in microelectronics fabrication using rare gas and electronegative gas mixtures are usually operated at a few to hundreds of mTorr pressures to process 300 mm wafers [15,16]. The radio frequency (RF) driven antennas (coils) use several configurations including spiral (flat, planar) and helical [17]. In the spiral-flat configuration, the antenna is separated from the plasma by a 1-5 cm thick dielectric window. The power is typically applied using frequencies of a few to tens of MHz. When operated in a continuous wave (CW) mode, the power deposition from the antenna to the plasma is a few hundred Watts to a few kW. When pulsing, the power pulse repetition frequency is from hundreds Hz to tens of kHz with a duty cycle (DC, the fraction of the pulse period when power is on) of 10-50%. The plasma densities are  $10^{10}$  - $10^{12}$  cm<sup>-3</sup> during the power-on part of the pulse [17,18]. Electron densities can decay several orders of magnitude during the power-off portion of the pulsed cycle depending on the electronegativity of the mixture and operating conditions.

Skin depth is the distance over which the power in electromagnetic waves is absorbed in a plasma. The collisional skin depth of plasma is  $\lambda_c = (c/\omega_e)(2\omega/v_m)^{1/2}$ , where c is the speed of light,  $\omega$  is the radian frequency of the incident wave,  $\omega_e$  is the electron plasma frequency and  $v_m$  is the electron momentum transfer collision frequency [19]. The electron plasma frequency is  $\omega_e = \sqrt{n_e q^2/(\varepsilon_0 m_e)}$ , where  $n_e$  is the electron density, q is the elementary charge,  $\varepsilon_0$  is the permittivity of free space, and  $m_e$  is electron mass. The collisional skin depth of plasma decreases with

the inverse square root of electron density. For electronegative pulsed plasmas such as Ar/Cl<sub>2</sub> gas mixtures, the electron density remaining at the end of the prior inter-pulse period before applying power for the following pulse may produce a longer skin depth than the size of the chamber. This condition prevents power from being efficiently absorbed in the plasma from the electromagnetic wave, which dominantly has an azimuthal electric field [17,20]. However, current passing through the antenna produces an inductive voltage drop across the antenna that results in electrostatic electric fields between the antenna and plasma, typically in the radial and axial directions. These electrostatic fields result in capacitive power coupling, typically known as the E-mode, where a significant fraction of the power is transferred to the ions in the sheath that forms at the window under the antenna [12,20–22].

E-mode power deposition results, in part, from oscillation of sheaths at surfaces bounding the plasma. Although power deposition into electrons in E-mode is small, it is not negligible. This power deposition heats electrons resulting in ionization that increases plasma density, which shortens the skin depth. As the skin depth shrinks to fit within the chamber, power deposition from the electromagnetic wave begins to dominate, which marks the transition to the H-mode [23]. Transitions between the electrostatic and inductive modes, referred to as E-H mode transitions, can occur at beginning of each power pulse during repetitively pulsed operation [10,24–26]. Depending on the antenna geometry and placement, and use of a Faraday shield, both E-mode and H-mode power deposition can simultaneously occur, even during CW operation and the quasi-steady state of a long power pulse.

In electronegative gas mixtures using pulsed power, the negative charge in the plasma prior to the application of power can be dominated by negative ions. Electronegativity (ratio of negative ion density to electron density) can be tens to hundreds at the end of the inter-pulse period. When power is applied to such a plasma, instabilities can occur. The instabilities associated in such electronegative ICPs include modulation of ion density propagating with the ion-acoustic speed, oscillations in charged particle density, electron temperature, and plasma potential for Ar/O<sub>2</sub> and Ar/SF<sub>6</sub> mixtures [9,10,27,28]. Lee and Chung investigated the hysteresis of E-to-H and H-to-E transitions by calculating the capacitively and inductively transferred powers and interpreted electron density dependence of the powers. They found that the electron densities and powers at the transitions are affected by the pressure and the chamber size [20]. Chabert et al. noted the importance of matching networks [10] during E-H transitions, as the impedance of the plasma (and

PLEASE CITE THIS ARTICLE AS DOI: 10.1063/5.0146168

### the ability to match power delivery to this impedance) changes significantly during the power-on period. In electronegative plasmas, negative ions are actively involved in maintaining charge neu-

In electronegative plasmas, negative ions are actively involved in maintaining charge neutrality. At the beginning of a power pulse having with high electronegativity, the plasma can be described as an ion-ion plasma where positive and negative ion densities are nearly in balance. For a purely ion-ion plasma with both charge carriers having the same mobilities and diffusivities, there is a negligible sheath at surfaces since the fluxes of negative and positive charge carriers to the surface balance. With application of power at the beginning of a pulse, an electron-ion plasma will be created at the edge of the ion-ion plasma where the evolving sheath motion heats electrons. This formation of a sheath dominantly occurs at the surface of the dielectric adjacent to the antenna. As the development of the sheath depends on the local electronegativity of the plasma, the spatial distribution of negative ions in the plasma at the start of the power pulse is important to the manner of initial power deposition and to the eventual E-H transition.

The behavior of plasma sheaths during the transition of the ion-ion to an electron-ion plasma has not been investigated in detail. Laser-induced fluorescence (LIF) and laser photodetachment have been used to probe this process [6]. Laser photodetachment of electrons from negative ions provides information on the spatiotemporal distributions of negative ions and their density. With sufficient laser intensity, electrons can be photo-detached from all ions in the focal volume [6]. The increase in the electron saturation current of an adjacent probe then provides a measure of the negative ion density [27,29].

The choice of gas in electronegative mixtures can have a significant effect on the E-H transition in low pressure, pulsed ICPs. In mixtures containing thermally attaching gases, such as Cl<sub>2</sub>, the decay in electron temperature during the inter-pulse period produces a rapid increase in the rate coefficient for electron attachment. This large rate coefficient produces a decrease in electron density and commensurate increase in the density of Cl<sup>-</sup>, producing electronegativities in the range of 1-100 [30,31]. For non-thermally attaching gases, such as O<sub>2</sub>, there is little dissociative attachment during the inter-pulse period, resulting in only a small increase in the electronegativity of the plasma [32,33].

In this paper, we discuss results from simulations and experiments to gain further insight into the E-H transitions that occur in pulsed electronegative ICPs for the conditions of interest to microelectronics materials processing. E-H transitions were computationally investigated for

pulsed ICPs sustained in Ar/Cl<sub>2</sub> and Ar/O<sub>2</sub> gas mixtures at pressures of tens of mTorr, average power deposition of hundreds of watts, and pulse repetition frequencies of 10-100 kHz with variable duty cycle. Although most pulsed ICPs used for microelectronics fabrication also use a bias on the substrate, we are not including such a bias in this study to focus attention on the E-H transition produced by antenna power alone. We found that argon-chlorine and argon-oxygen mixtures have different E- H mode transition behavior. The more rapid reduction in electron density during the afterglow period when using Ar/Cl<sub>2</sub> mixtures results in a higher impedance of the plasma at the onset of the power pulse compared to Ar/O<sub>2</sub> mixtures. Upon onset of power in the next pulse, this initially higher impedance results in a more dominant electrostatic component of power deposition, which launches electrostatic waves and produces energetic ion fluxes onto the dielectric window under the antenna. The cross-sectional shape of the antenna is also a factor in the E-H transition at the beginning of a power pulse. Inductive (H-mode) coupling to the plasma is weakly dependent on the shape of the antenna. However, electrostatic (E-mode) coupling does depend on the shape through the capacitance of the antenna relative to the plasma.

Brief descriptions of the computational platform used in this study, and the accompanying experiment are in Sec. II. Validation of the model is discussed in Sec. III. Results from computational investigations of E-H transitions for different duty cycles, pulse repetition frequency, gas mixture and antenna geometries are discussed in Section IV. Concluding remarks are provided in Sec. V.

### II. Description of the Model and ExperimentA. Description of the Model

These computational investigations of pulsed ICPs were conducted using the Hybrid Plasma Equipment Model (HPEM). Since a detailed discussion of HPEM can be found in a previous work [34], only a brief description of the modules used in this study will be provided here. The HPEM is a 2-dimensional modular plasma simulator where properties of the plasma, power delivery, and circuitry are addressed in different modules. Each individual module uses time slicing techniques to enable an appropriate timestep to be used in that module while interfacing with other modules on their appropriate timescales.

The modules in the HPEM used in this study are the Fluid Kinetics-Poisson Module (FKPM), the Electromagnetic Module (EMM), the Electron Energy Transport Module (EETM),

the Plasma Chemistry Monte Carlo Module (PCMCM) and the Circuit Module (CM). Electromagnetic fields ( $\vec{E}(\vec{r},t)$  and  $\vec{B}(\vec{r},t)$  with  $\vec{r}=(r,\theta,z)$ ) in the plasma resulting from RF current delivered to the antenna are computed in the EMM using plasma properties provided by other modules. The EMM includes a CM that is configured to represent a matchbox network to deliver power from a fixed impedance supply and cable to the plasma. The resulting currents through the antenna produce a voltage drop (amplitude and phase) which forms the basis of electrostatic coupling to the plasma. To solve the circuit equations in the CM, a capacitive impedance is required for the plasma. This impedance is obtained from the FKPM by Fourier analyzing the displacement current collected by the antenna. The voltages on the antenna produced by the CM are used in the FKPM as boundary conditions on the antenna elements in solving Poisson's equation for the electrostatic potential.

The trajectories of secondary electrons emitted from surfaces are tracked in the EETM using the electromagnetic fields from the EMM and electrostatic fields from the FKPM. The electron energy distributions of secondary electrons produced by collecting statistics on these trajectories are used to produce electron impact reaction rate coefficients and sources of electron charge deposited in the plasma. These secondary electron source terms are transferred to the FKPM where densities, momenta and temperature of heavy particles and bulk electrons are calculated using inductive power deposition from the EMM. Using the voltage boundary conditions on the antenna from the EMM, Poisson's equation is solved for the electric potential. Electrostatic fields from solution of Poisson's equation are Fourier analyzed to provide an impedance for current delivery from the antenna for use in the CM.

At low pressures (< 10 mTorr), nonlocal and non-collisional effects – mostly correlated with anomalous skin effects and stochastic heating – are expected in electron dynamics [35]. In this study, the electron temperature was produced using a continuity equation that captures non-local behavior through convection and conduction of electron energy density, though this is not performed kinetically. The trajectories of secondary electrons are followed using a Monte Carlo simulation that does include full kinetics effects. Simulations were performed at 10 mTorr in order to remain in a regime where these techniques are well applied.

With electromagnetic fields from the EMM, and electrostatic fields and source functions from the FKPM, ion energy and angular distributions striking surfaces in contact with the plasma are computed in the PCMCM. Using these source functions, the PCMCM launches pseudo-

PLEASE CITE THIS ARTICLE AS DOI: 10.1063/5.0146168

particles representing ions, and tracks them using Monte Carlo techniques. The distributions of energy and angles of these particles striking surfaces are recorded.

In RF powered systems, it is common to use an impedance matching network (IMN) between the plasma reactor and the cable from the power supply. The plasma reactor represents the load impedance which the IMN will match to the impedance of the power supply and connecting cable. The load impedance contains components from the physical inductance, capacitance and resistances of the structure of the chamber and antenna, and the impendence of the plasma. For an ICP, the impedance of the chamber is dominated by the inductance and resistance of the antenna, and the capacitance of the dielectric window between the antenna and the plasma. The impedance of the plasma dominantly depends on the plasma skin depth, conductivity of the bulk plasma and the sheath thickness at surfaces bounding the plasma (and particularly at the surface underneath the antenna). These factors depend on pressure, power, gas composition, geometry, and other operating conditions [36]. An impedance mismatch between the load (chamber and plasma) and that of the cable (transmission line) from the power supply results in reflection of power back to the supply, which is minimized by the IMN. The fraction of the electromagnetic wave amplitude delivered by the transmission line that is reflected from the plasma reactor in the absence of the IMN,  $\Gamma_{\rm E}$ , is

$$\Gamma_E = \frac{Z_L - Z_0}{Z_L + Z_0} \tag{1}$$

where  $Z_L$  is the combined impedance of the load represented by the physical properties of the reactor chamber and the plasma, and  $Z_0$  is the impedance of the cable, which is matched to the impedance of the power source. With the IMN, the load impedance also includes the parallel and serial impedances from IMN in series with the impedance of the reactor. The impedance of the power supply is typically 50  $\Omega$ , whereas that of the plasma reactor can be hundreds of ohms of both resistance and reactance [37]. The total power deposited into the IMN (having some finite resistance) and plasma reactor for a power delivery of  $P_S$  from the supply is

$$P_T = \left(1 - \left|\Gamma_E\right|^2\right) P_S \tag{2}$$

The circuit schematic used to represent the IMN and plasma reactor is shown in Fig. 1. The manner of incorporating the IMN into the plasma simulation is discussed by Qu et al.[38]. The circuit has five components: generator, matchbox, coil, plasma, and termination. The generator is represented by the power supply impedance, R<sub>G</sub>, which is matched to the cable interfacing to the

IMN, having impedance  $Z_0$ . The IMN has serial components of the matchbox resistance,  $R_M$ , and the capacitance,  $C_S$ . The parallel components are inductance,  $L_P$ , and parallel  $C_P$ . Matching of the load  $Z_L$  to  $Z_0$  is accomplished by varying the values of  $C_S$  and  $C_P$ . The plasma and antenna are also represented as serial and parallel impedances. The serial impedance includes the coil resistance,  $R_{CL}$  and inductance,  $L_{CL}$ ; and the transformed plasma resistance,  $R_{PL}$ , and inductance,  $L_{PL}$ . The parallel impedance is due to the capacitive coupling from the antenna to external components including the plasma. This impedance includes the capacitance of the air gap between the antenna and the dielectric window,  $C_C$ , sheath capacitance,  $C_S$ , and bulk plasma resistance,  $R_{BP}$ . The antenna is terminated to ground through inductance and capacitance represented by  $L_T$  and  $C_T$ . A discrete transmission line is used to model the antenna. The antenna impedance is distributed amongst individual segments in series that are mapped onto the turns of the coil.

The total power deposited into the chamber has capacitive, inductive, and resistive components. The capacitive coupled power delivered by the antenna to the plasma,  $P_C$ , is dominantly due to the electric fields (here in the (r,z) directions) produced by the voltage on the antenna. With the air gap between the antenna and dielectric window, and the window itself having negligible conductivity, these electric fields produce charged particle acceleration at the sheaths produced by RF oscillation of the plasma potential, and the resistive current losses for transmitting that capacitive current through the bulk plasma as conduction current. These dissipative losses are manifested by a phase offset in the displacement current that flows from the antenna. The capacitively coupled power is then a time average of the product of the antenna voltage and displacement current flowing from the antenna,

$$P_{C} = \sum_{i} \frac{1}{\tau_{RF}} \iint \varepsilon_{0} V_{i}(t) \frac{dE_{n}}{dt} dA dt$$
 (3)

where i is the number of turns in the antenna,  $\tau_{RF}$  is the period of RF power applied to the antenna,  $\varepsilon_0$  is the permittivity of free space,  $V_i$  is the voltage at each antenna turn,  $E_n$  is the normal component of the time-varying electric field at the surface of the antenna and A is the surface area of the coil.

The inductive power delivered by the antenna to the plasma due to inductively coupled fields  $\vec{E}(\vec{r})$  is,

$$P_{I} = \frac{1}{\tau_{RE}} \iint \vec{j} \left( \vec{r} \right) \cdot \vec{E} \left( \vec{r} \right) d^{3}r \, dt \tag{4}$$

PLEASE CITE THIS ARTICLE AS DOI: 10.1063/5.0146168

where  $\vec{j}(\vec{r})$  is the current density. For this 2-dimensional geometry  $\vec{E}(\vec{r})$  has only an azimuth component.

In addition to the inductive and capacitive power delivered by the antenna to the plasma, power is also dissipated by the resistance of the antenna,  $P_A$ , and of the components in the IMN,  $P_M$ . The power deposition in the plasma is then

$$P_{p} = P_{C} + P_{I} = P_{T} - P_{A} - P_{M} \tag{5}$$

The following circuit values were held constant during simulations unless otherwise noted. The total antenna inductance was 5.28  $\mu$ H and resistance 0.1  $\Omega$ . The termination values were  $L_T$  = 5 nH and  $C_T$  = 100 nF. The matchbox resistance was negligible (set to  $R_M$  = 1 $\mu\Omega$ ) and parallel inductance  $L_P$  = 0.1  $\mu$ H. The values of  $C_S$  and  $C_P$  were varied for matching as described below.

The reaction mechanism used for  $Ar/Cl_2$  plasmas is the same as that described in Ref.[39], and for  $Ar/O_2$  plasmas is the same as in Ref.[40]. The schematic of the cylindrically symmetric chamber used in the simulations is shown in Fig. 2c with the symmetry axis being at r=0 cm. The dielectric window underneath the antenna is divided into two regions that have identical material properties. The region below the antenna is that portion of the window on which ion energy and angular distributions (IEADs) are collected. The time to achieve a pulse-periodic steady state in the simulations is shortened by starting the simulations with CW power having the same value as the average power over the pulsed period. After achieving a quasi-steady state with CW power, several cycles of power pulse were simulated to reach the pulse periodic steady state. IEADs onto surfaces were calculated during the last pulse. There can be considerable gas heating and dissociation that can in turn produce variations in pressure. The pressure was held constant, here at 10 mTorr, by continuously adjusting the outlet flow rate.

### **B.** Description of the Experiment

Experimental measurements were performed in an ICP chamber originally part of an industrial HVM reactor. The chamber was modified to enable optical and electric probe access. Schematics of the experimental chamber are shown in Fig. 2a,b. The nominally cylindrically symmetric chamber is a metal, 52 cm in diameter and 17.2 cm tall, as measured from the surface of the wafer to the dielectric window. The antenna consists of a double-wound 1.5 turn stovetop coil powered by a 2 MHz RF generator that can be pulsed at arbitrary duty cycles. RF power delivered to the antenna was monitored by the voltage and current at its terminal. A 30 cm wafer is in contact

PLEASE CITE THIS ARTICLE AS DOI: 10.1063/5.0146168

with a ceramic chuck 45.5 cm in diameter. Gas enters the chamber, regulated by mass-flow controllers, through an inlet on the chamber wall, about 2 cm above the wafer and is pumped through an annulus surrounding the chuck. A pendulum valve connects the chamber and a turbopump.

Electric probes are mounted on a 3-dimensional drive and enter the chamber through a ball valve that allows free rotation. In this experiment, a three-dimensional magnetic B-dot probe was used to calculate current density and a hairpin probe was used to measure the electron density. The plasma was pulsed at 10 Hz, with a 10% duty cycle, and 300 W to 500 W input RF power. The gas pressure was 10 mTorr, with a total gas flow rate of 10 sccm.

The B-dot probe consisted of three single turn probes with a diameter 3.4 mm positioned closely together. Data was taken on half the r-z plane, assuming azimuthal symmetry. The loops picked up voltage induced by the magnetic field (dB/dt) in each direction [41]. The time series was recorded by an oscilloscope with 20 ns resolution. The magnetic field was calculated by taking the integral of the signal. The induced RF current in the azimuthal direction in the plasma can then be calculated by taking the curl of the magnetic field.

The hairpin probe is a quarter-wave resonator whose vacuum resonance frequency is 2.47 GHz. The resonance frequency shifts with the series impedance of the surrounding plasma and has a linear relation with the square root of the electron density. A circuit was developed to drive the resonator with a microwave signal and to detect the resonant response [42]. The resonance was found by sweeping a voltage ramp corresponding to a range of frequencies. The period of the ramp was  $10 \, \mu s$ .

### **III. Set Point Matching**

During pulsed operation of the ICP, the time scales of the changes in plasma impedance are typically shorter than the time that would be required to change the values of the components in the IMN to maintain a match. Therefore, the components in the IMN are typically set to values that match power at a particular time during the pulse cycle. This technique is known as set-point matching [38]. Choosing a set-point that matches early during the pulsed period will enable more power transmitted in the capacitive E-mode which dominates at the start of the pulse. Choosing a set point that matches late during the pulse period will enable more power transmitted in the inductive H-mode. Although choosing the set-point early in the pulse when capacitive power is high accelerates the ignition of the plasma, the poor match later in the pulse reduces total power

PLEASE CITE THIS ARTICLE AS DOI: 10.1063/5.0146168

deposition to the plasma throughout the pulse by reflecting power from the IMN during H-mode. While matching during the H-mode delays plasma ignition, more power is transmitted to the plasma overall.

The steps to determine the set-point matching values are briefly described for the base case plasma conditions. The base case, described in Table 1, is a pulsed ICP in an  $Ar/Cl_2 = 60/40$  gas mixture at 10 mTorr, with a pulse repetition frequency (PRF) of 13 kHz, duty cycle (DC) of 36% and 380 W pulse-averaged power. For a given set of operating conditions, a simulation was performed while continuously and instantaneously changing the values of the series capacitance of the IMN, C<sub>S</sub>, and parallel capacitance, Cp, to obtain perfect matching to the power supply throughout the pulse. This perfect matching is possible numerically but not experimentally. For example, C<sub>S</sub> and Cp are shown in Fig. 3a, with total power, inductive and capacitive power as a function of time. (Capacitive power is computed using Eq. 3. Inductive power is computed using Eq. 4.) Match point 1 is during the rise time in power, the E-mode, where the capacitive power is commensurate with inductive power. Match point 2 corresponds to the steady H-mode where the dominant power deposition is inductive. Values of C<sub>S</sub> and Cp are chosen for the desired set-point, and a second simulation is performed with these constant values of C<sub>S</sub> and Cp.

Power deposition, charged particle densities and electron temperature are shown in Figs. 3b,c, obtained with values of C<sub>S</sub> and C<sub>P</sub> at the match points 1 and 2 noted in Fig. 3a for the base case. Matching when the E-H mode transition is occurring (P1) produces earlier plasma ignition with more capacitive power at the leading edge of the pulse and lower reflected power. Although the reflected power is small during the power rise where matching is good, the reflected power increases up to 36% of the total power during the quasi-steady state H-mode. Matching while the H-mode is dominant (P2) produces a sharp peak in the reflected power up to 47% during the power rise time. The reflected power dissipates after achieving the H-mode. For this geometry, there is capacitive coupling and capacitive power deposition even during well matched H-mode operation. This capacitive coupling is due to the close proximity of the antenna to the window and plasma, and due to the lack of a Faraday shield. So, technically, the system operates in a mixed E- and Hmodes with the H-mode dominating. The capacitive power during the H-mode is larger with P2 matching than P1 matching. However, this is simply due to the larger total power deposition as the capacitive power is about 10% of the deposited power for both cases. In the remainder of this study, all cases use set-point patching at P2 which maximizes the total power deposition by

PLEASE CITE THIS ARTICLE AS DOI: 10.1063/5.0146168

matching during the quasi-steady H-mode.

The effects of a set-point matching on plasma properties are shown in Fig. 3c. Matching at P1 produces a faster rise of electron temperature with the chamber averaged T<sub>e</sub> reaching up to 5.4 eVs, about 0.5 eV higher than with P2 matching. Similarly, the average electron density rises earlier with P1 matching. However, P2 matching produces an electron density later in the pulse that is 50% higher than P1 matching due to the lower reflected power. The electronegativity of the plasmas is 12.5 for P1 matching and 9.8 for P2 matching.

### IV. Comparison with Experiment

A comparison of the simulation with experimental measurements was performed for an  $Ar/O_2 = 80/20$  mixture. The electron densities were measured with hairpin probes under the antenna. The antenna was powered at 2 MHz. The operating conditions were 10 mTorr, 10 Hz pulse repetition frequency with 10% duty cycle, and 100 sccm gas flow into the chamber. The region over which the plasma properties were measured is rectangular, 20 cm by 11 cm. The probe's location is shown in Fig. 2b, where the probe has translational and rotational motion capability. The measurements for electron density shown in Fig. 4 were obtained by keeping the azimuthal location constant.

With the low PRF, small duty cycle and long interpulse period, each pulse is essentially independent of the prior pulse. As a result, pulse periodic conditions were not explicitly computed. Instead, the cycle averaged power was applied to achieve a quasi-steady state. Power was then turned off after achieving a steady-state to let the plasma decay. Then, the power profile based on experiment measurements was applied for  $1004~\mu s$  to simulate that portion of the power pulse that was interrogated experimentally. During the simulations for comparison with the experiment, perfect matching was enforced. A comparison of simulated electron density with experiments at 104, 254, and  $1004~\mu s$  after start of the pulse is shown in Fig. 4. At these times, the reactor is operating dominantly in the H-mode. The experimental measurements are shown in Fig. 4a,b,c at t=104, 254, and  $1004~\mu s$ . The corresponding numerical simulations are shown in Fig. 4d,e,f at the same times. The measurement locations in the chamber are shown in Fig. 4g. The applied power profile in the simulation is shown in Fig. 4h. There was an overshoot in applied power in the experiments reaching up to 1300~W until  $250~\mu s$ . After the overshoot, the average power in the experiment remains constant at around 440~W. Since a matching network was not used in the experiment, the

average power in simulations was decreased to account for estimated losses due to reflection and resistance in circuit elements.

At 104  $\mu$ s, the peak electron density  $(0.1\text{--}3.0 \times 10^{10}~\text{cm}^{\text{--3}})$  is located near the top of the reactor under the antenna where the inductively coupled electric fields and electron temperature are the largest. As the pulse progresses, gas heating begins to rarefy the gas while excited states of Ar and  $O_2$  increase in density, which then enables multi-step ionization to begin to dominate. This then enables a transition of the peak in plasma density to move towards the center of the reactor. The magnitude of the electron density is well captured by the simulations. However, the movement of the plasma core towards the middle of the chamber starts earlier in the simulations. In the experiments, the central volume fills with plasma while retaining a maximum near the antenna. These differences may be explained by differences in the initial electron density distributions at the onset of power.

### V. Properties of Pulsed ICPs during E-H Transitions

Parametric studies were computationally performed to investigate the properties of pulsed ICPs experiencing E-H transitions. The consequences of gas mixture, duty cycle, pulse repetition frequency, and antenna geometry were examined. No bias was applied to the substrate in order to focus attention on the consequences of these parameters on the E-H transitions resulting from applying power to the antenna.

Ar/Cl<sub>2</sub> and Ar/O<sub>2</sub> electronegative gas mixtures were investigated as representatives of two modes of dissociative attachment. Cl<sub>2</sub> is a thermally attaching gas. The cross-section for electron impact dissociative attachment ( $e+Cl_2 \rightarrow Cl^- + Cl$ ) increases sharply for electron energies below 2 eV [43]. For an Ar/Cl<sub>2</sub> = 60/40 gas mixture, the rate coefficient for electron dissociative attachment is  $7.0 \times 10^{-10}$  cm<sup>3</sup>s<sup>-1</sup> at an electron temperature of 0.2 eV, decreasing to  $2.4 \times 10^{-10}$  cm<sup>3</sup>s<sup>-1</sup> at an electron temperature of 4 eV. Therefore, Cl<sup>-</sup> production rises when the electron temperature is lower, mostly during power-off portions of the cycle during the afterglow. As a result, the negative ion density typically increases during the afterglow.

Dissociative electron attachment to ground state O<sub>2</sub> has a threshold energy of 3.64 eV.

$$e + O_2\left(X^3 \sum_{g}^{-}\right) \to O_2^{-*} \to O^{-}\left({}^{2}P\right) + O\left({}^{3}P\right) \tag{5}$$

The threshold energy decreases for excited states of  $O_2$ , [44]. For an Ar/ $O_2 = 60/40$  gas mixture,

the rate coefficient for electron dissociative attachment is maximum at an electron temperature of about 4 eV with a value of  $5.2 \times 10^{-11}$  cm<sup>3</sup>s<sup>-1</sup>, decreasing with decreasing electron temperature. Significant O<sup>-</sup> production therefore typically occurs only during the power-on part of the pulse when the electron temperature is high. Dissociative attachment to O<sub>2</sub> is usually negligible during the power-off period. With ion-ion neutralization and associative detachment reactions occurring during the afterglow, which are independent of electron temperature, the negative ion density will usually decrease during the afterglow.

Power deposition, reflected power and plasma properties for the base pulsed ICP in Ar/Cl<sub>2</sub> = 60/40, 10 mTorr mixture are shown in Fig. 5a,b. The rise time of the power delivered from the supply is 4.5  $\mu$ s, reaching a maximum of 1050 W. This power is held constant until 27  $\mu$ s at which time the power is linearly decreased to zero in 4.5  $\mu$ s. Since the set point matching (P2) was selected for the quasi-steady H-mode, the reflected power peaks during the initial transient when power is applied. The magnitude of reflected power reaches 478 W during the ramp-up in power where the E-mode dominates. The reflected power diminishes to less than 7 W at around 10  $\mu$ s as the set-point values for C<sub>S</sub> and C<sub>P</sub> provide a better match to the H-mode. The rapid rise of the capacitive and reflective power as a fraction of the total delays the onset of inductive power deposition.

The consequences of capacitive coupling are shown by the oscillations in the plasma potential at the RF frequency. During the early portion of the pulse when the E-mode dominates, the plasma potential oscillates with an amplitude of 145 V. As the E-mode diminishes in relative importance and the H-mode begins to dominate, the amplitude of the oscillations in the plasma potential also diminish, in large part due to a decrease in the voltage across the antenna. This decrease in voltage is afforded by the increase in electron density (and plasma conductivity) during the power on period, from  $2.5 \times 10^9$  cm<sup>-3</sup> at the beginning of the pulse to  $2.8 \times 10^{10}$  cm<sup>-3</sup> at the end of the pulse. At mid-pulse capacitive power is 107 W, or 10% of the total power deposition.

Due to thermal attachment reactions with chlorine molecules, electron densities are low at the beginning of the power pulse as the electron density rapidly decays during the afterglow. Due to this initially low electron density, the electron temperature  $T_e$  spikes to 5 eV at the beginning of the pulse, a value higher than the steady state as needed to avalanche the gas.  $T_e$  decreases with the rise of electron density due to there being more electrons to dissipate the deposited power. The  $Cl^-$  density decreases during the pulse due to the high electron temperature which reduces its source

PLEASE CITE THIS ARTICLE AS DOI: 10.1063/5.0146168

while ion-ion neutralization depletes its density. At the end of the pulse, the densities of electrons and negative ions are about the same,  $2.8 \times 10^{10}$  cm<sup>-3</sup>, resulting in the dominant ion  $\text{Cl}_2^+$  having a maximum density of  $5.3 \times 10^{10}$  cm<sup>-3</sup>. During the afterglow, the electron density rapidly decays due to formation of  $\text{Cl}^-$  by dissociative attachment. In spite of this source of negative ions, the density of  $\text{Cl}^-$  increases by only 10-15%, as there are also losses due to ion-ion neutralization with positive ions, and  $\text{Cl}_2^+$  in particular.

Power distributions and the chamber averaged plasma properties for a pulsed ICP for the  $Ar/O_2 = 60/40$ , 10 mTorr mixture are shown in Figs. 5c,d. As with the Ar/Cl<sub>2</sub> mixture, P2 set point matching was used for the H-mode. The magnitude of the reflected power at the beginning of the pulse peaks at 380 W or about 60% of the 650 W delivered by the supply. At the time, the inductive power is about 200 W and capacitive power is about 70 W. The reflected power diminishes to < 3 W by 5.2 µs when the delivered power reaches a steady state, more than twice as fast as the Ar/Cl<sub>2</sub> mixture. At this time, both capacitive and inductive power also achieve their quasi-steady state. Unlike the Ar/Cl<sub>2</sub> mixture, the electron density for the Ar/O<sub>2</sub> mixture does not decay significantly during the afterglow with O production occurring dominantly in the power-on part of the pulse. The large electron density at the beginning of the pulse,  $2.2 \times 10^{10}$  cm<sup>-3</sup>, enables a more rapid onset of the H-mode. As a result, the initial oscillation the plasma potential, 98 V, is smaller than for the Ar/Cl<sub>2</sub> mixture. With the electron density and plasma conductivity increasing by only about 18% during the pulse, the antenna current also does not significantly change during the Hmode. As a result, the antenna voltage remains nearly constant and so the oscillation in the plasma potential is also nearly constant. At mid-pulse capacitive power is 153 W, or 15% of the total power deposition, with the remainder being dominantly being inductive power deposition. With the P2 match, the reflected power is negligible.

With the initially larger electron density,  $T_e$  has a smaller initial spike, remaining between 3.8 eV and 3.6 eV during the pulse. The electron density increases slowly due in part to its density being already large enough to dissipate the desired power and due to losses to generate  $O^-$ , whose density increases during the power pulse. The dominant positive ion is  $O_2^+$ . During the afterglow, the electron density decreases by only 18% as dissociative attachment of  $O_2$  falls to negligible values with the decrease in  $T_e$ . [45]

During the afterglow of the Ar/Cl<sub>2</sub> mixture, the plasma transitions to an ion-ion plasma, which results in a shrinking of the sheaths adjacent to all surfaces. When power is applied to the

antenna, the voltage across the antenna increases and capacitive coupling to the plasma ramps up, the response of the plasma is to form a sheath to dissipate the capacitive voltage. The sheath is initially formed by expelling what electrons remain from the boundaries of the plasma at surfaces, with each cycle of the applied voltage. These actions produce electrostatic waves that emanate from surfaces.

The electron density and the electrostatic waves for the Ar/Cl<sub>2</sub> base case are shown in Fig. 6 at times: 3.0  $\mu$ s (mixed E-H mode), 7.5  $\mu$ s (early H-mode), 25.5  $\mu$ s (steady H-mode), and 60.0  $\mu$ s (power-off part of the pulse). The color contours show the electron density. The black lines show where the charge density  $\rho = 0$  with labels indicating the charge density in units of  $10^7$   $\rho/q$  cm<sup>-3</sup>. The amplitude of the voltage on the antenna for each turn is indicated.

At the end of the prior pulse, the electron density has decayed to  $3 \times 10^9$  cm<sup>-3</sup>, the while C1<sup>-</sup> density has risen to  $3.5 \times 10^{10}$  cm<sup>-3</sup>. The power coupling from the antenna is initially capacitive. Since the mobilities of negative and positive ions are of the same order and smaller than that of electrons, the ions do not move quickly to generate the sheath under the antenna. Therefore, the large potentials under the antenna expel the low-density electrons from the boundaries near surfaces over a distance of a few mm, producing electrostatic waves (Fig. 6a). These waves propagate with wave fronts that are largely parallel to the bottom and side boundaries with amplitudes of  $\Delta p/q = 0.5$ - $10 \times 10^7$  cm<sup>-3</sup>. In the lower right corner of the reactor the wave fronts are distorted, a consequence of the intersection of waves launched from the surfaces of the side wall and focus ring. The waves at the surface of the top window appear to emanate dominantly from under the innermost turn of the antenna where the voltage is the largest, and the need to form a sheath is the greatest. The charge density is largest in the sheath under the antenna where the sheath potential is the largest.

As the H-mode begins (Fig. 6b) and the electron density (and conductivity) increase, the voltage on the antenna begins to decrease and the sheaths thin. The electron density at first increases under the antenna where both modes of power deposition (E- and H-mode) are largest. The launching of the electrostatic waves diminishes. Deep in the H-mode (Fig. 6c) when the electron densities in excess of  $10^{10}$  cm<sup>-3</sup> have spread throughout the reactor, the launching of waves with oscillation of the plasmas potential due to capacitive coupling has essentially ceased. What waves remain are due to prior cycles, having reflected from surfaces and been slowly damped. Due to the thermal attachment reactions, electrons are mostly consumed at the ion-ion core of the

PLEASE CITE THIS ARTICLE AS DOI: 10.1063/5.0146168

plasma and remain primarily at the boundary of the core plasma at the end of the pulse, as shown in Fig. 6d.

Electron and charge densities for the Ar/O<sub>2</sub> base case are shown in Fig. 7 for the same times as for the Ar/Cl<sub>2</sub> base case of Fig. 6. Upon applying power and producing a voltage across the antenna, a sheath forms at surface and particularly under the antenna. Since the electron densities at the beginning of the pulse are large (>  $10^{10}$  cm<sup>-3</sup>), the sheath can form while making a small perturbation in the nearby electron densities, and no significant electrostatic waves are launched. Charge densities remain small and positive in the bulk plasma, as needed to maintain the positive plasma potential. There is a larger positive charge density near the wall under the antenna as needed to form the sheath that dissipates the capacitive voltage from the antenna. There is little change in these configurations during the pulse as the plasma is largely in the H-mode from the start of the power pulse.

### a) Gas Mixtures

The electronegativity of the plasma contributes to the intensity of the E-H transition. More electronegative gas mixtures translate to smaller electron densities and larger impedance at the beginning of a power pulse. The larger impedance then initially emphasizes the E-mode. These trends are demonstrated by varying the halogen mole fractions in the  $Ar/Cl_2$  mixture from  $Ar/Cl_2$  = 100/0 to  $Ar/Cl_2$  = 10/90. For each case, set-point matching was used for the H-mode (P2) resulting in different values of  $C_S$  and  $C_P$ . For gas mixtures containing only 10% of the halogen in argon, the majority of power deposition by electron collisions occurs dominantly with the halogen.

The capacitive, inductive, and reflected powers for different gas compositions are shown in Fig. 8a for Ar/Cl<sub>2</sub>. Plasma potential and electron density are shown in Fig. 8b. With increasing Cl<sub>2</sub> fraction, the peak electron density decreases at the end of the power pulse, from  $4.8 \times 10^{10}$  cm<sup>-3</sup> for pure Ar to  $1.9 \times 10^{10}$  cm<sup>-3</sup> for Ar/Cl<sub>2</sub> = 10/90. The increasing rate of dissociative attachment during the afterglow with increasing Cl<sub>2</sub> mole fraction decreases the electron density at the beginning of the next pulse from  $3.3 \times 10^{10}$  cm<sup>-3</sup> for pure Ar to  $6.0 \times 10^7$  cm<sup>-3</sup> for Ar/Cl<sub>2</sub> = 10/90. The resulting increase in impedance at the beginning of the power pulse results in oscillations of the plasma potential of an excess 1000 V for Ar/Cl<sub>2</sub> = 10/90 to 86 V for pure Ar.

The plasmas with higher mole fractions of Cl<sub>2</sub> and higher initial impedances begin the pulse clearly in the E-mode. However, there is not a clear trend with reflected power. While the pure

argon case has the largest reflected power peak (577 W), the second largest reflected power for  $Ar/Cl_2 = 50/50$  is 511 W. The smallest reflected power is 184 W for  $Ar/Cl_2 = 80/20$ . This non-monotonic behavior is likely a result of set point matching for the H-mode. That said, there is generally a delay in the onset of the H-mode inductive power deposition with increasing  $Cl_2$  mole fraction. Since set-point matching at P2 is being used, the total power deposition (inductive and capacitive) is essentially the same at the end of the pulse regardless of  $Cl_2$  mole fraction.

With the values of C<sub>S</sub> and C<sub>P</sub> chosen to match in the H-mode (P2) for each gas mixture, there is no guarantee that the unmatched behavior at the beginning of the will follow systematic trends with Cl<sub>2</sub> mole fraction. The general trends are that larger Cl<sub>2</sub> mole fractions produce larger reflected powers during the initial E-mode with more delayed onset of the H-mode. The split between capacitive and inductive power in the H-mode favors more capacitive power for lower Cl<sub>2</sub> mole fractions. However, given the small initial electron densities at high Cl<sub>2</sub> mole fractions with varying spatial distributions, there is a stochastic component for how high mole fraction systems start with each pulse.

The capacitive, inductive, and reflected powers for different gas  $Ar/O_2$  compositions are shown in Fig. 8c. Plasma potential and electron density are shown in Fig. 8d. Similar to  $Ar/Cl_2$  mixture, the increase in the  $O_2$  fraction produces a decrease in electron density at the end of the power pulse, from  $4.8 \times 10^{10}$  cm<sup>-3</sup> for pure Ar to  $2.1 \times 10^{10}$  cm<sup>-3</sup> for  $Ar/O_2 = 20/80$ . For the same gas fractions (20/80), the ratios of the electron density at its maximum value to the electron density at the end of the pulse are 1.3 for  $Ar/O_2$  and 115 for  $Ar/Cl_2$ . Due to the smaller decay of the electron density during the afterglow, the E-H transitions at the beginning of the next power pulse are smoother for  $Ar/O_2$  mixtures. The bulk plasma oscillations rise from 86 V for pure Ar to 140 V for pure  $O_2$ . With the larger pre-pulse electron densities, even for operating with pure  $O_2$ , the  $Ar/O_2$  mixtures are able to void the large oscillations in plasma potential as experienced with  $Ar/Cl_2$  mixtures. With the H-mode (P2) matching, the capacitive power deposition at the match point is generally larger for the  $Ar/O_2$  mixtures than for  $Ar/Cl_2$  mixtures, with the gas mixtures with the large molecular mole fractions having more capacitive coupling.

The electron temperature and electronegativity during the pulse for  $Ar/Cl_2$  mixtures are shown in Fig. 9a. The electronegativity of the plasma at the beginning of the power pulse ranges from 19 for  $Ar/Cl_2$ = 80/20 to 580 to  $Ar/Cl_2$ = 10/90. Higher electronegativities correlate to higher electron temperatures at the leading edge of the pulse in order to avalanche the gas. The electron

density and  $\rho = 0$  contours (indicating electrostatic waves) for Ar/Cl<sub>2</sub>= 20/80 and 50/50 shown in Fig. 9b at a times of 1.5  $\mu$ s and in Fig. 9c for 3.3  $\mu$ s. With the larger Cl<sub>2</sub> mole fraction, the electron density under that antenna at the beginning of the power pulse is 0.3 -1.2  $\times$  10<sup>8</sup> cm<sup>-3</sup>, with a local electronegativity of 245-400. For all practical purposes, this is an ion-ion plasma. Upon application of power, producing a voltage drop across the antenna, electrostatic waves are nearly immediate launched. With the Ar/Cl<sub>2</sub>= 50/50 mixture, the electron density under the antenna at the beginning of the power pulse is 0.7-1.6  $\times$  10<sup>8</sup> cm<sup>-3</sup>. This electron density is just sufficient to sustain the sheath under the antenna at early times during power pulse when the inner-most antenna voltage is 1030 V at 1.5  $\mu$ s. However, as the antenna voltage increases to 1240 V at 3.3  $\mu$ s, the sheath cannot be sustained, and electrostatic waves are launched to extend the width of the sheath.

The E-H transition is ultimately sensitive to the rate of electron avalanche that increases electron density and decreases the electromagnetic skin depth. There are several contributions to the electron avalanche that vary with both gas mixtures ( $Cl_2$  or  $O_2$ ) and mole fraction. For example, Penning ionization has been proposed as a major contributor to ionization, and to the E-H transition in Ar/Hg mixtures [46], a system in which all excited states of Ar can Penning ionize Hg and there is no attachment. Penning ionization of  $Cl_2$  (ionization potential = 11.45 eV) is just accessible to all Ar excited states (energy of lowest state  $Ar(1s_5) = 11.55$  eV) whereas Penning ionization of  $O_2$  (IP = 12.1 eV) is only accessible by Ar(4p) and higher states [47]. Multi-step ionization from excited states of Ar decreases during the E-H transition due to quenching of these states, a process that increases with increasing  $Cl_2$  or  $O_2$  mole fraction. During the E-H transition where the electron temperature tends to be maximum, the rate coefficient for attachment to  $O_2$  generally increases whereas that for  $Cl_2$  decreases with increasing  $T_e$ .

### b) Duty Cycle and PRF

For the same PRF (13 kHz) and operating conditions, the consequences of duty cycle (DC, fraction of pulse period power is applied) on plasma properties were investigated. The average power was kept constant while changing the duty cycle and so pulses with shorter duty cycles have higher peak powers. Three duty cycles were investigated, 12.5, 25, and 50%, with peak powers of  $P_0 = 2800$ , 1400, and 700 W to provide a cycle averaged power of 350 W.

The normalized power distributions (P/P<sub>0</sub>) and chamber averaged electron densities and plasma potentials are shown in Fig 10a,b for the Ar/Cl<sub>2</sub> mixture for different duty cycles. Set-point

matching for the H-mode (P2) was used. There is not enough time for the capacitive and inductive power to reach steady states for the shortest duty cycle. As such, the set point matching for the H-mode is not effective. Operating with larger DC enabled achieving steady power distributions. With decreasing DC, there is more opportunity for the electrons to thermally attach to  $Cl_2$  during the longer afterglow to produce  $Cl^-$ , which results in a decrease in electron density at the beginning of the power pulse and increase in electronegativity. The electron density at the beginning of the pulse is  $1.5 \times 10^9$  cm<sup>-3</sup>,  $2.3 \times 10^9$  cm<sup>-3</sup> and  $4.7 \times 10^9$  cm<sup>-3</sup> for duty cycles of 12.5, 25, and 50%. The corresponding electronegativities at the end of the pulse are 28, 15, and 7 for duty cycles of 12.5, 25, and 50%. The end result is a longer skin-depth and more resistive plasma at the beginning of the power pulse for low duty cycle, leading to a greater proportion of E-mode coupling. For example, the oscillation in the plasma potential at the start of the pulse reaches 325 V, 218 V and 107 V for duty cycles of 12.5, 25, and 50%.

The normalized power distributions (P/P<sub>0</sub>) and chamber averaged electron densities and plasma potentials are shown in Fig 10c,d for the  $Ar/O_2$  mixture for different duty cycles. With the  $Ar/O_2$  mixture not being thermally attaching the electron densities at the beginning of the power pulse are  $4.0 \times 10^{10}$  cm<sup>-3</sup>,  $2.8 \times 10^{10}$  cm<sup>-3</sup> and  $1.6 \times 10^{10}$  cm<sup>-3</sup> for duty cycles of 12.5, 25, and 50%. Electronegativity decreases during the afterglow due to the lack of thermal attaching processes, whereas for the  $Ar/Cl_2$  mixture the electronegativity increases. The corresponding electronegativities at the end of the pulse are 0.05, 0.1, and 0.3 for duty cycles of 12.5, 25, and 50%. With the plasma conductivity remaining high throughout the afterglow, the E-H transition at the start of the pulse occurs rapidly for all DC. Both the E- and H-mode power deposition achieves a steady state even for the smallest DC.

When changing PRF with constant duty cycle and average power, the peak power remains the same. Higher PRF produces both shorter power-on and afterglow periods. PRFs of 10, 50, and 100 kHz, with pulse lengths of 100, 20, and 10  $\mu$ s were investigated. The chamber averaged electron, Cl<sub>2</sub><sup>+</sup> and Cl<sup>-</sup>, and power distributions for the Ar/Cl<sub>2</sub> mixture are shown in Fig. 11a,b for different PRF. The horizontal axis is time normalized by the total pulse length. Since a 10 kHz pulse has both longer power-on and power-off times, the initial electron density at the beginning of the power pulse is smaller,  $1.7 \times 10^9$  cm<sup>-3</sup> with larger modulation during the pulse period than at the higher PRFs. The electron density at 10 kHz varies by a factor of 20 during the pulse whereas at 50 kHz and 100 kHz, the electron density varies by less than 34%. When using H-mode (P2)

matching, the mis-match at the beginning of the power pulse is therefore larger with lower PRF, resulting in reflected power for 10 kHz reaching 500 W with a delay in the start of the H-mode. Since electron densities exceed  $1.4 \times 10^{10}$  cm<sup>-3</sup> at the start of the pulse at the higher PRF, the reflected power is small, with H-mode starting with the onset of power. The H-mode (P2) matching applies for nearly the entire pulse. The quasi-steady-state capacitive power is the smallest for the highest frequency.

The chamber averaged electron, O<sub>2</sub><sup>+</sup> and O<sup>-</sup>, and power distributions for the base case Ar/O<sub>2</sub> mixture are shown in Fig. 12a,b for different PRF. The horizontal axis time normalized by the pulse length for 10, 50, and kHz having pulse lengths of 100, 20, and 10 μs. Similar to Ar/Cl<sub>2</sub> mixture, the lower PRF produces the largest ion densities. The electron density does not significantly decrease during the afterglow due to lack of a strong loss mechanism such as thermal attachment. The electron density at 10 kHz varies by a factor of 1.6, whereas at 50 kHz and 100 kHz, the electron density varies by a factor less than 10%. Lower electron production at higher frequencies results in larger reflected power at the beginning of the pulse, as shown in Fig. 12b. The delay in the onset of the H-mode is similar to the Ar/Cl<sub>2</sub> mixture. The slower rise of inductive power deposition at the higher frequency with H-mode (P2) matching results in more reflected power (and less capacitive power).

### c) Cross Sectional Profile of the Antenna

The spiral antenna used in stove-top ICP systems is often constructed by shaping metal stock having a rectangular cross section. In principle, the H-mode inductive coupling should not be particularly sensitive to the cross-sectional shape of antenna. The RF magnetic field produced by the antenna depends only on the enclosed current. So for positions at least several coil diameters away from the antenna, the RF magnetic field should be nearly independent of the shape of the antenna. (Here, the term diameter is being used to describe the average width of the rectangular cross section of the antenna.) That said, the E-mode capacitive coupling depends on the displacement current collected by the antenna which, to first order, is proportional to the area of the face of the antenna directed towards the plasma. With this expectation, antennas with cross sections having larger areas facing the plasma will likely have more capacitive coupling.

The consequences of antenna having different cross section profiles were investigated for ICPs sustained in Ar/Cl<sub>2</sub> and Ar/O<sub>2</sub> mixtures. For otherwise the base case operating conditions,

PLEASE CITE THIS ARTICLE AS DOI: 10.1063/5.0146168

the antenna profiles shown in Fig. 13e were investigated. On the left side of Fig. 13e, the profile of the antenna in the r- $\theta$  plane is shown — the sketch is not to the scale. The model represents a three-turn antenna as three separate rectangular sections on each side of the axial line of symmetry [48]. The antenna is powered on the inner end (1') and grounded at the outer end (3) through a termination capacitance of 100 nF. The profile A0 is the base case antenna configuration with a 1.5 cm wide and 1.44 cm high cross section producing an aspect ratio (width/height) of AR = 1.05. (Larger AR has a wider surface facing the plasma.) The more squat antenna, A1, has the same width but half of the height of A0 with AR=2.09. The wider antenna A2 configuration has the same height but 50% more width than A0, with AR = 1.57. Lastly, the thinner antenna A3 has the same height and half of the width of A0, with AR = 0.52. The inductance of these antennas are 5.3  $\mu$ H for the base case A0, 5.52  $\mu$ H for shorter antenna A1, 4.61  $\mu$ H for the wider A2 and 6.0  $\mu$ H for the thinner A3.

The consequences of antenna cross section on the power distributions, reactor averaged electron density, and plasma potentials for Ar/Cl<sub>2</sub> mixture are shown in Fig. 13a,b. H-mode (P2) matching was employed, resulting in small reflected power late in the pulse for all antennas. However, the distribution of capacitive-vs-inductive power is sensitive to the antenna cross section. The largest capacitive power, 200 W or 19% of the total, is produce with the widest antenna, A2. Since the surface area facing the plasma is largest, more displacement current flows through the antenna, which then contributes to capacitive coupling. Similarly, A3 has the smallest surface facing the plasma and results in the smallest capacitive power, 83 W or 8% of the total. The height of the antenna, and so aspect ratio, does not significantly affect the power distribution. However, decreasing the height of the antenna height (larger AR) produces a decrease in the total surface area which can collect displacement current, which causes a small reduction in capacitive power. The displacement current to the sides of the antenna is dominated by the radial electric field E<sub>r</sub> which typically has a smaller magnitude than the axial electric field, E<sub>z</sub>. E<sub>r</sub> also has a component due to a voltage difference between turns of the antennal, producing displacement current that is exchanged between turns of the antenna, which largely cancel each other. For example, A0 and A1 have the same widths, while, A1 has the larger aspect ratio. The capacitive power for A0 is marginally larger than for A1.

The correlation of capacitive power with plasma-facing area of antenna is reflected in the oscillation of the plasma potential. Antenna A2 (largest area) produces the largest capacitive

oscillation in the plasma potential of 194 V, while antenna A3 (smallest area) produces the smallest oscillation in the plasma potential of 110 V. Antennas producing the smallest E-mode power deposition (largest H-mode) generally produce the largest electron densities, though this effect is not large (6.4% difference in electron density between A2 and A3.)

Although the E-mode vs H-mode power deposition late in the pulse correlate with the plasma facing area of the antennas, it is difficult to define a similar trend in the reflected powers or rate of H-mode power rise. Those antennas producing the smallest E-mode power late in the pulse (smallest plasma facing area, smallest AR) have the largest reflected power at the start of the pulse. For example, A0 and A3 have maximum reflected power of 460 W, while A1 and A2 have reflected powers of 150 W and 200 W. This counter-intuitive trend is an artifact of the H-mode (P2) matching. The P2 matching with smaller E-mode power in the steady state is less able to accept the negative reactance of capacitive coupling at the beginning of the pulse. With negative reactance dominating at the start of the pulse, the result is more reflected power.

The consequences of antenna geometry on the power distribution, chamber averaged electron density, and plasma potentials for the  $Ar/O_2$  mixtures are shown in Fig. 13c,d. The trends with antenna cross section profile are essentially the same as with the  $Ar/Cl_2$  mixture – antennas with larger plasma facing area produce more E-mode power deposition and more oscillation in the plasma potential. Since the electron densities at the beginning of the pulse for the  $Ar/O_2$  mixture are 4-5 times larger than the  $Ar/Cl_2$  mixture, the onset of the H-mode is more rapid with less severe oscillation in the plasma potential at the beginning of the pulse.

### d) IEADs onto the Wafer and Window

The oscillation of the plasma potential due to E-mode coupling largely results from voltage dropped across the sheath at the plasma facing surfaces. E-mode power is dominantly electrostatic with a significant fraction of the power transferred to ions by acceleration through the sheaths. With the sheath voltage drop being largest at the window directly under the antenna, the window is often eroded along the path of the antenna [45]. Etched or sputtered particles from the window can then affect the selectivity of etching, and the repeatability of the process. Different methods have been investigated to weaken the capacitive coupling, including Faraday shields, axial magnetic fields, and antennas with lower inductance and so smaller inductive voltage drop that leads to electrostatic coupling [8]. Faraday shields reduce the erosion of the dielectric window by

reducing sheath voltage which translates to lower ion energies striking the window. However, Faraday shields can also result in difficulty in restarting the plasma at the beginning of the pulse when some capacitive coupling is useful to offset the large skin depth resulting from low electron densities [49]. To investigate E-mode-produced ion acceleration into surfaces, the ion energy and angular distributions (IEADs) incident onto the window and wafer were computed. IEADs were collected on the windows surface directly under the antenna (as shown in Fig. 2c) and averaged over the wafer. A bias on the substrate is the most effective way to control IEADs onto the wafer. However, this study is focused on those IEADs resulting strictly from E-mode coupling of the antenna without a bias on the substrate [6].

IEADs incident onto the window and wafer for the base case are shown in Figs 14 (Ar/Cl<sub>2</sub>) and 15 (Ar/O<sub>2</sub>) at different times during the power pulse – at the E-H transition (3.0 μs), early H-mode (7.5 μs), steady-H mode (25.5 μs), the ramp-down of power pulse (31.5 μs), and the end of the power pulse (36.0 μs). These times are shown by the vertical gray dashed lines in Fig. 5. The IEADs consist of the sum of all positive ions (Ar<sup>+</sup>, Ar<sub>2</sub><sup>+</sup>, Cl<sup>+</sup>, and Cl<sub>2</sub><sup>+</sup> for the Ar/Cl<sub>2</sub> mixture; Ar<sup>+</sup>, Ar<sub>2</sub><sup>+</sup>, O<sup>+</sup>, and O<sub>2</sub><sup>+</sup> for the Ar/O<sub>2</sub> mixture) averaged over the surface, plotted with a logarithmic scale over three decades. The normalized ion energy distributions (IEDs),  $f(\varepsilon)$  are also provided.

The IEADs and IEDs for the Ar/Cl<sub>2</sub> base case striking the window under the antenna are shown in Fig. 14a and 14c. The ions onto the window have energies up to 225 eV during the E-H transition (3.0  $\mu$ s) when the voltage amplitude on the innermost antenna is 1250 V, and maximum plasma potential is 83 V. With the capacitance of the window being 16 nF/cm<sup>2</sup>, the surface of the window quickly charges to -122 V under the turn of the antenna having the largest voltage. The potential difference between the plasma potential and surface of the window accounts for the range of ion energies, 10 to 225 eV with a narrow angular distribution ( $\pm$ 17°). With the onset of the H-mode (7.5  $\mu$ s), the antenna voltage decreases to 1203 V, plasma potential decreases to 81 V and charging of the dielectric is -105V, producing a commensurate decrease in maximum ion energy (185 eV) and broadening of the angular distribution ( $\pm$ 27°). During the steady H-mode (25.5  $\mu$ s), there is still capacitive coupling (antenna voltage, 1180 V, plasma potential 76 V) with charging of the surface of the window (-96 V), producing an IEAD onto the window of up to 185 eV. As the power pulse terminates (31.5  $\mu$ s) the decreasing antenna voltage and discharging of the surface of the window, lowers the ion energy onto the window (70 eV), further broadening the angular distribution ( $\pm$ 40°). In the early afterglow (36.0  $\mu$ s) with there being no voltage on the antenna,

PLEASE CITE THIS ARTICLE AS DOI: 10.1063/5.0146168

the dielectric window is simply an electrically floating surface, with the ions arriving at the surface with an energy up to the floating potential (10 eV) and a nearly isotropic angular distribution.

The IEADs and IEDs for the  $Ar/Cl_2$  base case striking the wafer are shown in Fig. 14b and 14c. The conductive wafer sits on a metal electrode terminated to the ground. With there being little charging and voltage drop across the wafer, the maximum energies of the IEADs striking the wafer are a measure of the maximum sheath potential above the wafer, whose upper limit is the plasma potential. The plasma potential is at its maximum value (98 V) at 4.5  $\mu$ s, which correlates with the maximum energy of the IEAD.

The IEADs onto the window and wafer for the  $Ar/O_2$  base case for different times during the power pulse are shown in Fig. 15. The delayed rise of capacitive power for the  $Ar/O_2$  base case, as shown in Fig. 4c, produces a delay for ion energies to reach their maximum values, as shown in Fig. 15a,c. The highest ion energies with narrow angular distribution striking the dielectric window occurred at 7.5  $\mu$ s. In the steady state H-mode, ion energies decrease, and angles broaden, similar to the  $Ar/Cl_2$  base case. The IEADs on the wafer have broad angular distributions at 3.0  $\mu$ s since the ions originate somewhat distant from the sheath edge, which itself undergoes oscillations. The angular distribution onto the wafer narrows during the H-mode with higher energies as the sheath at the surface of the wafer stabilizes. The decrease in energy reflects the decrease in antenna voltage.

The IEADs at 7.5 and 25.5  $\mu$ s contain an angularly narrow, high energy component of small magnitude. (The images in Fig. 15a are plotted over a 3-decade log-scale. This high energy peak would not be visible on a 2-decade log-scale.) These high energy peaks are due to  $O^+$ , and are case specific. For comparison, IEADs for individual ions at 25.5  $\mu$ s are shown in Fig. 16. With the  $O^+$  being the lightest ion in the mixture,  $O^+$  transport across the sheath is in the thin-sheath limit, which enables the  $O^+$  to arrive on the substrate with an energy corresponding to a larger fraction of the sheath potential.

The total IEDs incident onto the window at 3.0  $\mu$ s for Ar/Cl<sub>2</sub> mixtures and 7.5  $\mu$ s for Ar/O<sub>2</sub> mixtures are shown in Fig. 17. These times were chosen based on the IEADs having the highest energies. The energy range for pure argon is 20 eV to 160 eV at 3.0  $\mu$ s, with a peak around 110 eV. For the Ar/Cl<sub>2</sub> = 20/80 mixture, the range of energies extends to >250 eV. The increase in Cl<sub>2</sub> concentration and increase in electronegativity of plasma produces large oscillations in the plasma potential during the E-H transition (see Fig. 8a), which translates to a larger sheath potential

PLEASE CITE THIS ARTICLE AS DOI: 10.1063/5.0146168

and higher incident ion energies. The details of the shape of the IEDs are case specific. As shown in Fig. 6a, the sheath under the window has contributions from voltages on all three turns of the antenna, each of which has different phases. The sheath thickness is inversely proportional to electron density, producing a concave sheath edge during the E-H transition. The non-sinusoidal oscillation of a sheath having a non-planar shape while being transited by ions of multiple masses result in these complex IEDs. It is difficult to cite systematic trends for these conditions.

The IEDs onto the window for the Ar/O<sub>2</sub> mixtures show similar scaling as the Ar/Cl<sub>2</sub> mixtures with perhaps having higher order. For the pure O<sub>2</sub> mixture, the IED extends to 325 eV, whereas for the pure Ar mixture the IED extends to 175 eV. With the electron density under the antenna being higher (thinner sheath) and more uniform (flatter sheath edge) than with Ar/Cl<sub>2</sub> mixtures, as shown in Fig. 7, the IEDs are arguably more systematically varying with mixture. The thinner sheaths during the E-H transition produce a larger range of ion energies.

The time at which the IEADs onto the wafer have their maximum energy is 7.5  $\mu$ s for both gas mixtures. The IEADs onto the wafer for Ar/Cl<sub>2</sub> mixtures are shown in Fig. 18a and in 18b for Ar/O<sub>2</sub> mixtures for this time. There is no clear correlation between gas composition and the shape of IEADs striking the wafer for chlorine mixtures. The angular symmetry of the IEADs decreases with the addition of chlorine due to the still large resistivity and non-uniformity of the bulk plasma at 7.5  $\mu$ s. The low electron density near the sheath edge produces a thick sheath with a large voltage amplitude due to capacitive coupling, particularly at high Cl<sub>2</sub> mole fraction. Charge exchange and elastic collisions in the thick sheath produce a broad angular distribution. It is only for dilute gas mixtures, Cl<sub>2</sub> fractions less than 20%, than the sheath is thin enough for ion transport to approach the thin-sheath limit, identified by the 2-peak IED.

The larger pre-pulse electron density for the  $Ar/O_2$  mixtures results in the sheath above the wafer to always be in the near-thin-sheath limit. The IEDs have the characteristic 2-peak distribution for all mixtures. The IEDs have widths of about 20 eV with average energies of 45 - 70 eV, commensurate with the oscillation in the plasma potential with respect to ground.

The larger the antenna surface facing the plasma, the more significant the capacitive coupling will be. IEADs incident onto the dielectric window are shown in Fig. 19 for the widest (A2) and thinnest (A3) antennas for the  $Ar/Cl_2$  and  $Ar/O_2$  mixtures when the ion energies are at their maximum values (3.0  $\mu$ s for  $Ar/Cl_2$  and 7.5  $\mu$ s for  $Ar/O_2$ ). The conditions are otherwise the base case. For both mixtures, the flatter antenna which emphasizes the E-mode produces IEADs onto

PLEASE CITE THIS ARTICLE AS DOI: 10.1063/5.0146168

the window that have higher maximum energies and narrower angular distributions. The differences in the IEADs between the widest and thinnest antennas are less significant for the  $Ar/O_2$  mixtures. This trend results from the larger initial electron density and smoother E-H transition.

### VI. Concluding Remarks

During pulsed operation of ICPs as used for semiconductor fabrication, the electron density decreases during the inter-pulse due to diffusion, attachment and recombination. In molecular, attaching gas mixtures, the electron density may decrease to the degree that the plasma must be reignited at the beginning of each power pulse. These conditions lead to there being an E-H transition at the onset of power for each pulse. Results from numerical investigations of these E-H transitions were discussed for pulsed ICPs sustained Ar/Cl<sub>2</sub> and Ar/O<sub>2</sub>, mixtures that are highly attaching during the interpulse afterglow (Ar/Cl<sub>2</sub>) and nearly non-attaching (Ar/O<sub>2</sub>). E-H transitions were investigated for gas mole fractions, duty cycle, pulse repetition frequency, and antenna structures. IEADs onto the dielectric window under the antenna and onto the wafer were computed. Using set-point techniques, matchbox components were chosen to minimize reflected power at the end of the power pulse when the H-mode is in a quasi-steady state. This matching maximizes the pulse-averaged production of reactive species. With matching optimized to the H-mode late in the pulse, reflected power is maximum at the leading edge of the pulse when the E-mode dominates.

The thermally attaching nature of chlorine results in larger reductions in electron densities during the power off part of the pulse compared to Ar/O<sub>2</sub> mixtures. Due to the lower electron densities at the beginning of pulses, Ar/Cl<sub>2</sub> mixtures are prone to severe E-H transitions with a delay before reaching the quasi-steady-state. As a result, reflected powers for Ar/Cl<sub>2</sub> mixtures generally have larger magnitude and longer duration compared to Ar/O<sub>2</sub> mixtures. The severity of the E-H transition is measured, in part, by the magnitude of the oscillation in the plasma potential. Larger halogen mole fractions, larger plasma facing area of the antenna and shorter duty-cycles result in larger E-mode coupling, particularly at the beginning of the power pulse. For the conditions of this study, there is finite E-mode power dissipation in the quasi-steady state when H-mode dominates. This E-mode power typically increases with halogen mole fraction and for antennas with larger areas facing the plasma.

One consequence of severe E-H transitions for conditions where the plasma density is low is the launching of electrostatic waves in the plasma from beneath the antenna at the onset of power.

Waves are launched in Ar/Cl<sub>2</sub> mixtures and less so, if at all, in Ar/O<sub>2</sub> mixtures. These waves occur when the antenna voltage is large and the plasma has transitioned to nearly an ion-ion plasma during the afterglow. For these conditions, the sheath that forms under the antenna is thick, expelling the remaining electrons. The strength of the electrostatic waves increases with increasing electronegativity. The launching of the waves dissipates as the plasma density increases and sheath thins, and the voltage amplitude on the antenna decreases.

The oscillation of the plasma potential due to E-mode coupling results in energetic ion bombardment of all surfaces in contact with the plasma, and particularly so for the dielectric window beneath the antenna. Ion energies onto surfaces are largest during the E-mode when the oscillation in the plasma potential is the largest. For the conditions examined, ion energies in excess of 200 eV are incident onto the window. Ion energies onto the window during the E-H transition generally scale with the electronegativity of the gas mixture. The oscillation of the plasma potential also produces energetic ion bombardment of the wafer independent of a separately applied bias.

To minimize the consequences of the E-H transition at the beginning of power pulses in ICPS, there is a minimum electron density, on order of several times 10<sup>9</sup> cm<sup>-3</sup>, that should remain in the vicinity of the antenna at the start of the next power pulse. For the duty cycles and gas mixtures of interest, particularly when using thermally attaching gases, this may not be possible with power on-power off formats. High power-low power formats where a *keep-alive* electron density is maintained may be one strategy to reduce the severity of the E-H transition, concurrent with antenna designs that minimize the plasma facing area of the coils. The spatial uniformity with which the electron density decays during the power-off afterglow also factors into the severity of the E-H transition. The distribution of pre-pulse electron density may produce evolving sheaths with boundaries that are not parallel to surfaces, which produces ion bombardment of surfaces at non-normal angles. The angular distribution of ions may not be overly important for ions incident onto the dielectric window, but could be important for ions incident onto the wafer.

### **Conflict of Interest**

The authors have no conflicts to disclose.

### **Data Availability**

The data that support the findings of this study are contained within this paper and available

from the corresponding author upon reasonable request.

### Acknowledgements

This work was supported by the National Science Foundation (PHY-2009219), Lam Research Inc. and Samsung Electronics Ltd.

the online version of record will be different from this version once it has been copyedited and typeset

PLEASE CITE THIS ARTICLE AS DOI: 10.1063/5.0146168

This is the author's peer reviewed, accepted manuscript. However,

### References

- [1] K. J. Kanarik, J. Vac. Sci. Technol. A 39, 010401 (2021).
- [2] D. J. Economou, J. Phys. D. Appl. Phys. 47, 303001 (2014).
- [3] B. Wu, A. Kumar and S. Pamarthy, J. Appl. Phys. 108, 051101 (2010).
- [4] K. J. Kanarik, T. Lill, E. A. Hudson, S. Sriraman, S. Tan, J. Marks, V. Vahedi and R. A. Gottscho, *J. Vac. Sci. Technol. A* 33, 020802 (2015).
- [5] Y. Mitsui and T. Makabe, *Plasma Sources Sci. Technol.* **30**, 23001 (2021).
- [6] V. M. Donnelly and A. Kornblit, J. Vac. Sci. Technol. A 31, 50825 (2013).
- [7] S. B. Wang and A. E. Wendt, J. Appl. Phys. 88, 643 (2000).
- [8] M. Schaepkens, N. R. Rueger, J. J. Beulens, X. Li, T. E. Standaert, P. J. Matsuo and G. S. Oehrlein, *J. Vac. Sci. Technol. A* 17, 3272 (1999).
- [9] M. Tuszewski, J. Appl. Phys. 79, 8967 (1996).
- [10] P. Chabert, A. J. Lichtenberg, M. A. Lieberman and A. M. Marakhtanov, *Plasma Sources Sci. Technol.* **10**, 478 (2001).
- [11] M. A. Lieberman, A. J. Lichtenberg and A. M. Marakhtanov, *Appl. Phys. Lett.* **75**, 3617 (1999).
- [12] U. Kortshagen, N. D. Gibson and J. E. Lawler, J. Phys. D. Appl. Phys. 29, 1224 (1996).
- [13] T. Wegner, C. Küllig and J. Meichsner, *Plasma Sources Sci. Technol.* **26,** 025006 (2017).
- [14] X. Zhang, Z. Zhang, J. Cao, Y. Liu and P. Yu, AIP Adv. 8, 035121 (2018).
- [15] K. Tokashiki, H. Cho, S. Banna, J.-Y. Lee, K. Shin, V. Todorow, W.S. Kim, K. Bai, S. Joo, J.D. Choe, K. Ramaswamy, A. Agarwal, S. Rauf, K. Collins, S. Choi, H. Cho, H. J. Kim, C. Lee, D. Lymberopoulos, J. Yoon, W. Han and J.-T. Moon, *Jpn. J. Appl. Phys.* 48, 08HD01 (2009).
- [16] A. Agarwal, P. J. Stout, S. Banna, S. Rauf and K. Collins, *J. Vac. Sci. Technol. A* **29**, 11017 (2011).
- [17] J. Hopwood, Plasma Sources Sci. Technol. 1, 109 (1992).
- [18] D. Rauner, S. Briefi and U. Fantz, Plasma Sources Sci. Technol. 26, 095004 (2017).
- [19] J. Hopwood, et al., J. Vac. Sci. Technol. A 11, 147 (1993).
- [20] M.-H. Lee and C.W. Chung, *Phys. Plasmas* 13, 63510 (2006).
- [21] J. Amorim, H. S. Maciel and J. P. Sudano, J. Vac. Sci. Technol. B 9, 362 (1991).
- [22] S.X. Zhao, X. Xu, X.C. Li and Y.N. Wang, J. Appl. Phys. 105, 083306 (2009).
- [23] M. M. Turner and M. A. Lieberman, Plasma Sources Sci. Technol. 8, 313 (1999).
- [24] M. Edamura and E. C. Benck, J. Vac. Sci. Technol. A 21, 470 (2003).
- [25] C. Xue, F. Gao, D.Q. Wen and Y.-N. Wang, J. Appl. Phys. 125, 023303 (2019).
- [26] J. Han, P. Pribyl, W. Gekelman and A. Paterson, *Phys. Plasmas* 27, 063509 (2020)
- [27] C. S. Corr, P. G. Steen and W. G. Graham, *Plasma Sources Sci. Technol.* 12, 265 (2003).
- [28] C. S. Corr, E. Despiau-Pujo, P. Chabert, W. G. Graham, F. G. Marro and D. B. Graves, J. Phys. D. *Appl. Phys.* **41**, 185202 (2008).
- [29] C. B. Fleddermann and G. A. Hebner, J. Vac. Sci. Technol. A 15, 1955 (1997).
- [30] G. A. Hebner and C. B. Fleddermann, J. Appl. Phys. 82, 2814 (1997).

PLEASE CITE THIS ARTICLE AS DOI: 10.1063/5.0146168

- [31] M. V Malyshev, V. M. Donnelly, J. I. Colonell and S. Samukawa, *J. Appl. Phys.* **86,** 4813 (1999).
- [32] M. W. Kiehlbauch and D. B. Graves, J. Vac. Sci. Technol. A 21, 660 (2003).
- [33] M. Tadokoro, A. Itoh, N. Nakano, Z. L. Petrovic and T. Makabe, *IEEE Trans. Plasma Sci.* **26,** 1724 (1998).
- [34] M. J. Kushner, J. Phys. D. Appl. Phys. 42, 194013 (2009).
- [35] G. J. M. Hagelaar, *Plasma Sources Sci. Technol.* 17, 025017 (2008).
- [36] D. Sudhir, M. Bandyopadhyay, W. Kraus, A. Gahlaut, G. Bansal and A. Chakraborty, *Rev. Sci. Ins.* **85**, 13510 (2014).
- [37] J. B. Hagen, *Radio-Frequency Electronics*, Cambridge University Press (2009).
- [38] C. Qu, S. J. Lanham, S. C. Shannon, S. K. Nam and M. J. Kushner, *J. Appl. Phys.* **127**, 133302 (2020).
- [39] P. Tian and M. J. Kushner, Plasma Sources Sci. Technol. 26, 24005 (2017).
- [40] S. Huang, V. Volynets, J. R. Hamilton, S. Lee, I.C. Song, S. Lu, J. Tennyson and M. J. Kushner, *J. Vac. Sci. Technol. A* **35**, 031302 (2017).
- [41] X. Fan, Y. Wug, J. Han, P. Pribyl and T. Carter, Rev. Sci. Inst. 91, 113502 (2020).
- [42] Y. Wug, X. Fan, S. Mackie, P. Pribyl and T. Carter, AIP Advances, JP10.018 (2019).
- [43] W. Tam and S. F. Wong, J. Chem. Phys. **68**, 5626 (1978).
- [44] V. Laporta, R. Celiberto and J. Tennyson, *Phys. Rev. A* **91**, 12701 (2015).
- [45] N. Forgotson, V. Khemka and J. Hopwood, J. Vac. Sci. Technol. B 14, 732 (1996).
- [46] X. Zhang, P.C. Yu, Y. Liu, Z. Zheng, P. Wang and J. X. Cao, *Phys. Plasmas* **22**, 103509 (2015).
- [47] NIST. (2021). Atomic Spectra Database. Retrieved from https://www.nist.gov/pml/atomic-spectra-database
- [48] F. W. Grover, *Inductance calculations: working formulas and tables*, Dover (1962).
- [49] J. Hopwood, Plasma Sources Sci. Technol. 3, 460 (1994).

PLEASE CITE THIS ARTICLE AS DOI: 10.1063/5.0146168

### **Figure Captions:**

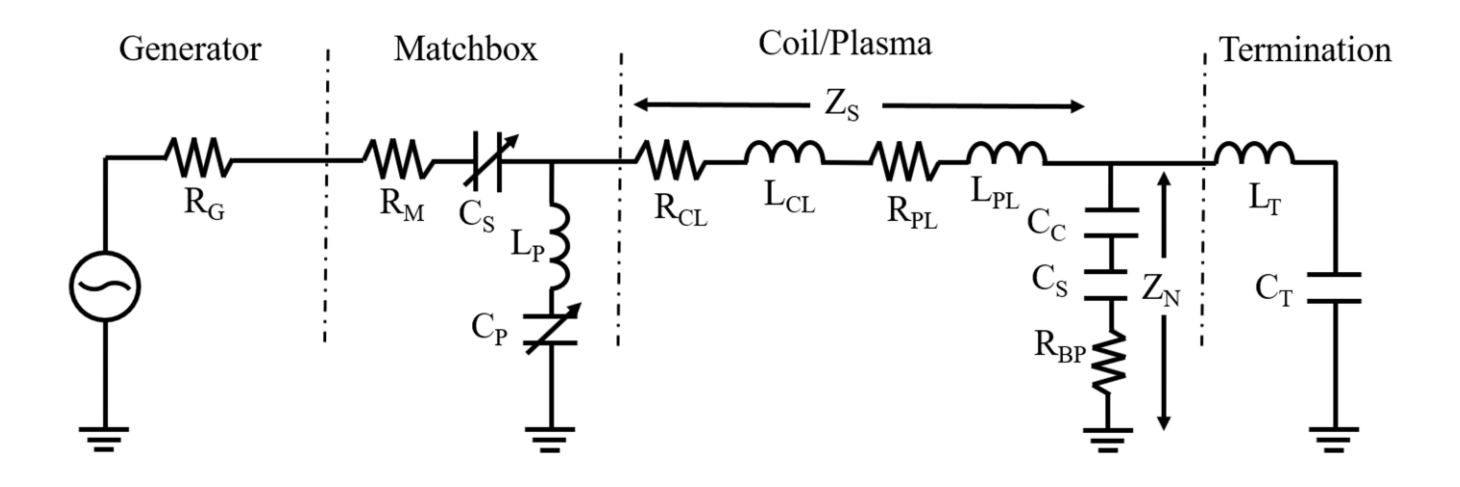
- 1. Schematic of the match box circuitry transmission line model for the antenna and reactor.
- 2. (Color Online) The experimental setup and schematic of the model cylindrical inductively coupled plasma reactor. a) Schematic of the experimental ICP chamber. b) Top view of the wafer and substrate. c) Schematic of the cylindrically symmetric computational domain.
- 3. (Color Online) Set point matching process for the Ar/Cl<sub>2</sub> base case simulation. a) Total power, inductive and capacitive power distributions with perfectly matched parallel (C<sub>P</sub>) and serial (C<sub>S</sub>) capacitance are shown through one pulse period. Points 1 (t = 3.8 μs) and 2 (t = 25.7 μs) represent set point matching at the E-H transition and during H-mode portions of the pulsed cycle. b) Inductive, capacitive, and reflected powers when using Point 1 (P1) and Point 2 (P2) values for C<sub>P</sub> and C<sub>S</sub>. c) Chamber averaged species densities and electron temperature through one pulse period.
- 4. (Color Online) Comparison of numerical simulation and experimental hairpin probe data for electron density in the ICP chamber for an Ar/O<sub>2</sub> = 80/20 mixture at 10 mTorr. Experimental data at a) 85  $\mu$ s and b) 940  $\mu$ s. Simulation results at c) 25  $\mu$ s, d) 85  $\mu$ s and e) 940  $\mu$ s. f) The location in the reactor for measurements. Electron density contours are linearly scaled with the given ranges. Lines show electron density ( $10^{10}$  cm<sup>-3</sup>).
- 5. (Color Online) Base cases (Table 1) comparisons of Ar/Cl<sub>2</sub> and Ar/O<sub>2</sub> mixtures. For Ar/Cl<sub>2</sub>: a) modes of power deposition and b) chamber averaged electron and ion densities and electron temperature, T<sub>e</sub> for Ar/Cl<sub>2</sub> mixture. For Ar/O<sub>2</sub>: a) modes of power deposition and b) chamber averaged electron and ion densities and electron temperature, T<sub>e</sub> for Ar/Cl<sub>2</sub> mixture. Dashed grey lines represent times referred to in Fig. 14-15.
- 6. (Color Online) Electron (color contours) and charge (lines) densities at various times during a pulsed period for the Ar/Cl<sub>2</sub> mixture. Electron densities are linearly scaled with the given maximum values. a)  $t=3~\mu s$ . b)  $t=7.5~\mu s$ . c)  $t=25.5~\mu s$ . d)  $t=60.0~\mu s$ . The charge density  $\rho$  is shown by labels in units of  $10^7$  q (1.6 x  $10^{-19}$  C/cm<sup>-3</sup>) with lines indicating  $\rho=0$ .
- 7. (Color Online) Electron (color contours) and charge (lines) densities at various times during a pulsed period for the Ar/O<sub>2</sub> mixture. Electron densities are linearly scaled with the given maximum values. a)  $t=3 \mu s$ . b)  $t=7.5 \mu s$ . c)  $t=25.5 \mu s$ . d)  $t=60.0 \mu s$ . The charge density  $\rho$  is shown by labels in units of  $10^7$  q (1.6 x  $10^{-19}$  C/cm<sup>-3</sup>) with lines indicating  $\rho=0$ .
- 8. (Color online) The consequences of gas mole fractions on the power deposition and the

- chamber averaged plasma properties. For Ar/Cl<sub>2</sub>: a) inductive, capacitive, and reflected powers; and b) chamber averaged electron density and bulk plasma potentials. For Ar/O<sub>2</sub>: c) inductive, capacitive, and reflected powers; and d) chamber averaged electron density and bulk plasma potentials. The notation, for example, 80/20 is for an Ar/Cl<sub>2</sub> = 80/20 or Ar/O<sub>2</sub> = 80/20 gas mixture.
- 9. (Color Online) Plasma properties for Ar/Cl<sub>2</sub> mixtures. a) Chamber averaged electronegativity and electron temperature through one pulse period. Electron (color contours) and charge (lines) densities for (left) Ar/Cl<sub>2</sub> = 20/80 and (right) Ar/Cl<sub>2</sub> = 50/50 during the rise time of the power at a) t= 1.5  $\mu$ s and b) t= 3.3  $\mu$ s. The charge density  $\rho$  is shown by labels in units of  $10^7$  q (1.6 x  $10^{-19}$  C/cm<sup>-3</sup>) with lines showing  $\rho$  = 0. The notation, for example, 80/20 is for an Ar/Cl<sub>2</sub> = 80/20 gas mixture.
- 10. (Color online) The consequences of duty cycle (DC) on the power deposition and the chamber averaged plasma variables. For Ar/Cl<sub>2</sub>: a) inductive, capacitive, and reflected powers; and b) chamber averaged electron density and plasma potentials. For Ar/O<sub>2</sub>: c) inductive, capacitive, and reflected powers; and d) chamber averaged electron density and plasma potentials. Powers are normalized with the peak powers of 2800, 1400, and 700 W for 12.5, 25, and 50% DC, respectively. The subscript on electron density signifies the duty cycle.
- 11. (Color Online) Plasma properties for different pulse repetition frequencies  $Ar/Cl_2$ . a) Chamber averaged electron and ion densities. b) Inductive, capacitive, and reflected powers. The x-axis is a normalized time for 10, 50, and 100 kHz, normalized with pulse lengths of 100, 20, and 10  $\mu$ s.
- 12. (Color online) Plasma properties for different pulse repetition frequencies Ar/O<sub>2</sub>. a) Chamber averaged electron and ion densities. b) Inductive, capacitive, and reflected powers. The x-axis is a normalized time for 10, 50, and 100 kHz, normalized with pulse lengths of 100, 20, and 10 μs.
- 13. (Color Online) Consequences of the shape of the antenna on plasma properties. For Ar/Cl<sub>2</sub>: a) modes of power deposition and b) electron densities and plasma potentials. For Ar/O<sub>2</sub>: c) modes of power deposition and d) electron densities and plasma potentials. e) Flat spiral antenna representation and cross sections of the different antenna configurations. The labels on curves in a) to d) refer to the antenna shapes shown in e).
- 14. (Color Online) Time variation IEADs resulting from summing fluxes of Ar<sup>+</sup>, Ar<sub>2</sub><sup>+</sup>, Cl<sup>+</sup>, and

- Cl<sub>2</sub><sup>+</sup> for the base case conditions onto a) the dielectric window under the antenna and b) the wafer. c) IEDs (integrated over angle) onto the window and wafer. The IEADs are on a log scale over 3 decades.
- 15. (Color Online) Time variation IEADs resulting from summing fluxes of Ar<sup>+</sup>, Ar<sub>2</sub><sup>+</sup>, O<sup>+</sup>, and O<sub>2</sub><sup>+</sup> for the base case conditions onto a) the dielectric window under the antenna and b) the wafer.
  c) IEDs (integrated over angle) onto the window and wafer. The IEADs are on a log scale over 3 decades.
- 16. (Color Online) IEADs for individual species onto the wafer at 25.5 μs. The plots are log-scaled over 3 decades.
- 17. (Color Online) The total IEDs on the dielectric window under the antenna for a) Ar/Cl<sub>2</sub> gas mixtures at 3.0  $\mu$ s and b) Ar/O<sub>2</sub> mixtures at 7.5  $\mu$ s. The notation, for example, 80/20 is for an Ar/Cl<sub>2</sub> = 80/20 or Ar/O<sub>2</sub> = 80/20 gas mixture.
- 18. (Color Online) The variations of total ion IEADs onto the wafer for a)  $Ar/Cl_2$  gas mixtures and b)  $Ar/O_2$  gas mixtures at 7.5 µs. c) IEDs (angle integrated IEADs) for the same conditions. The notation, for example, 80/20 is for an  $Ar/Cl_2 = 80/20$  or  $Ar/O_2 = 80/20$  gas mixture.
- 19. (Color Online) The consequences of antenna shape on IEADs (3-decade log-scale) onto the dielectric window under the antenna for the widest (A2) and thinnest (A3) antennas. For Ar/Cl<sub>2</sub> at 3.0 μs. a) wide (A2) and b) thin (A3). For Ar/Ol<sub>2</sub> at 7.5 μs. a) wide (A2) and b) thin (A3).

### **Table 1: Operating Conditions**

Gas Mixture	Ar/Cl <sub>2</sub> and Ar/O <sub>2</sub>
Base Case	(60/40), PRF: 13 kHz, 36% DC, 10 mTorr, 380 W (average), 10 MHz RF, antenna A0
Gas Composition (/)	(100/0 or 90/10), (80/20), (50/50), (20/80), (100/0)
Pulse Repetition Frequency (PRF)	10 kHz, 50 kHz, 100 kHz
Duty Cycle (DC)	12.5%, 25%, 50%
Antenna Geometry (A#)	Base(A0), Shorter(A1), Wider(A2), Thinner (A3)



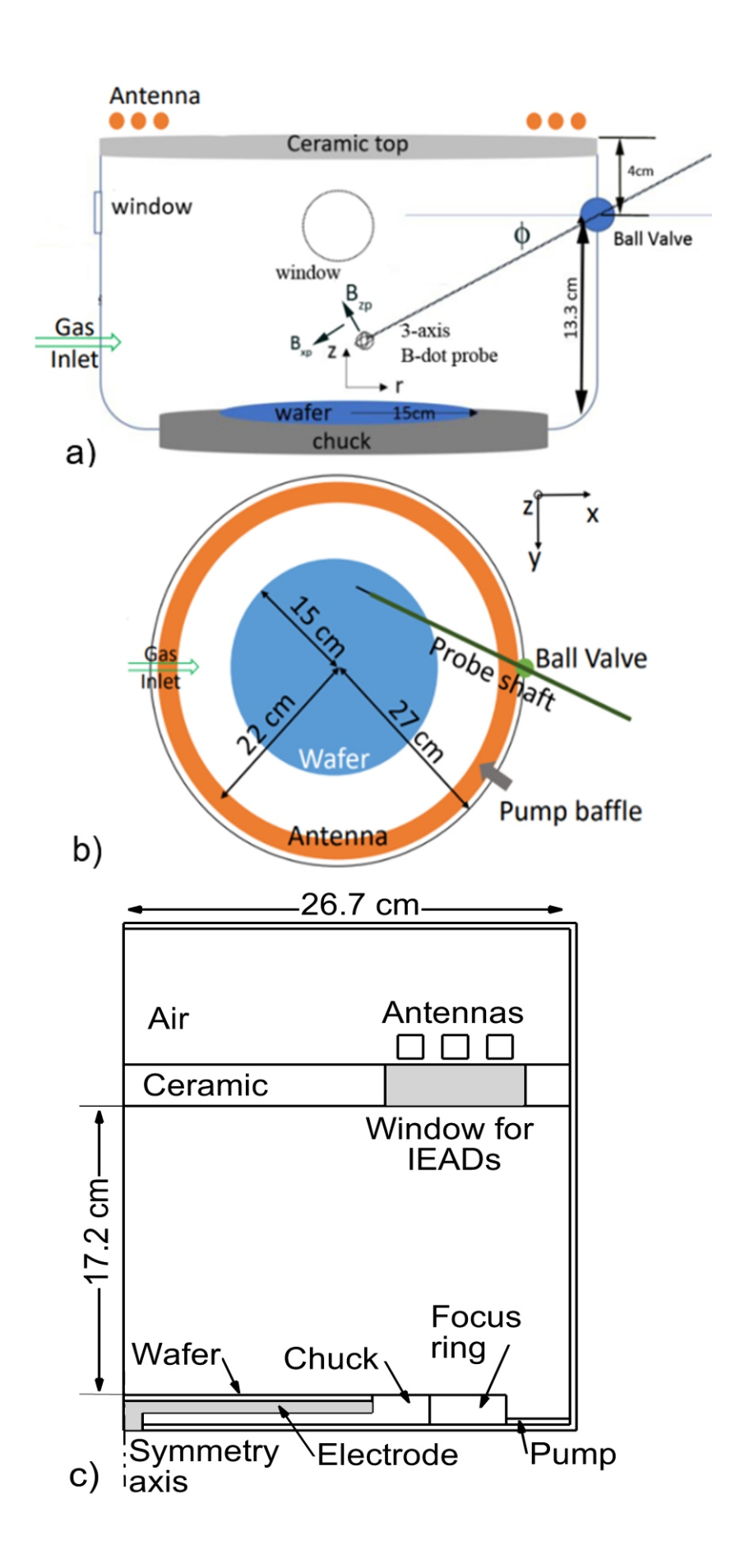


Figure 2 of 19

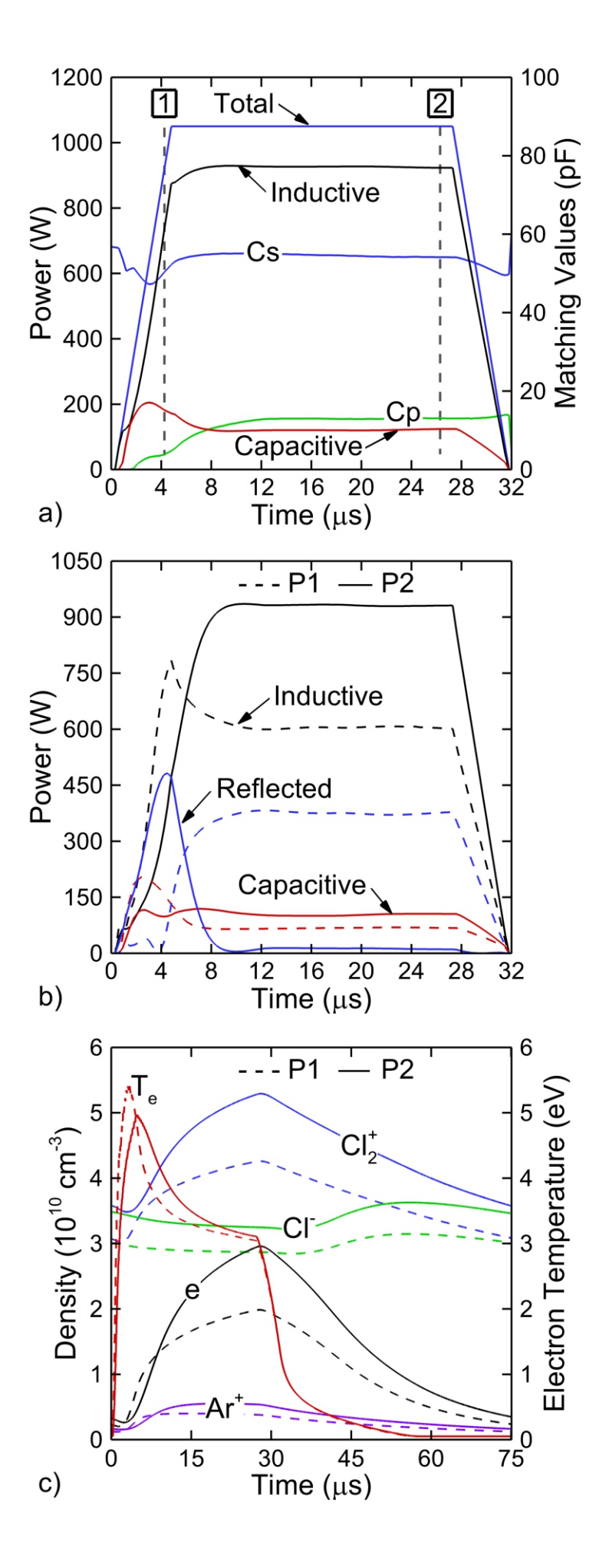
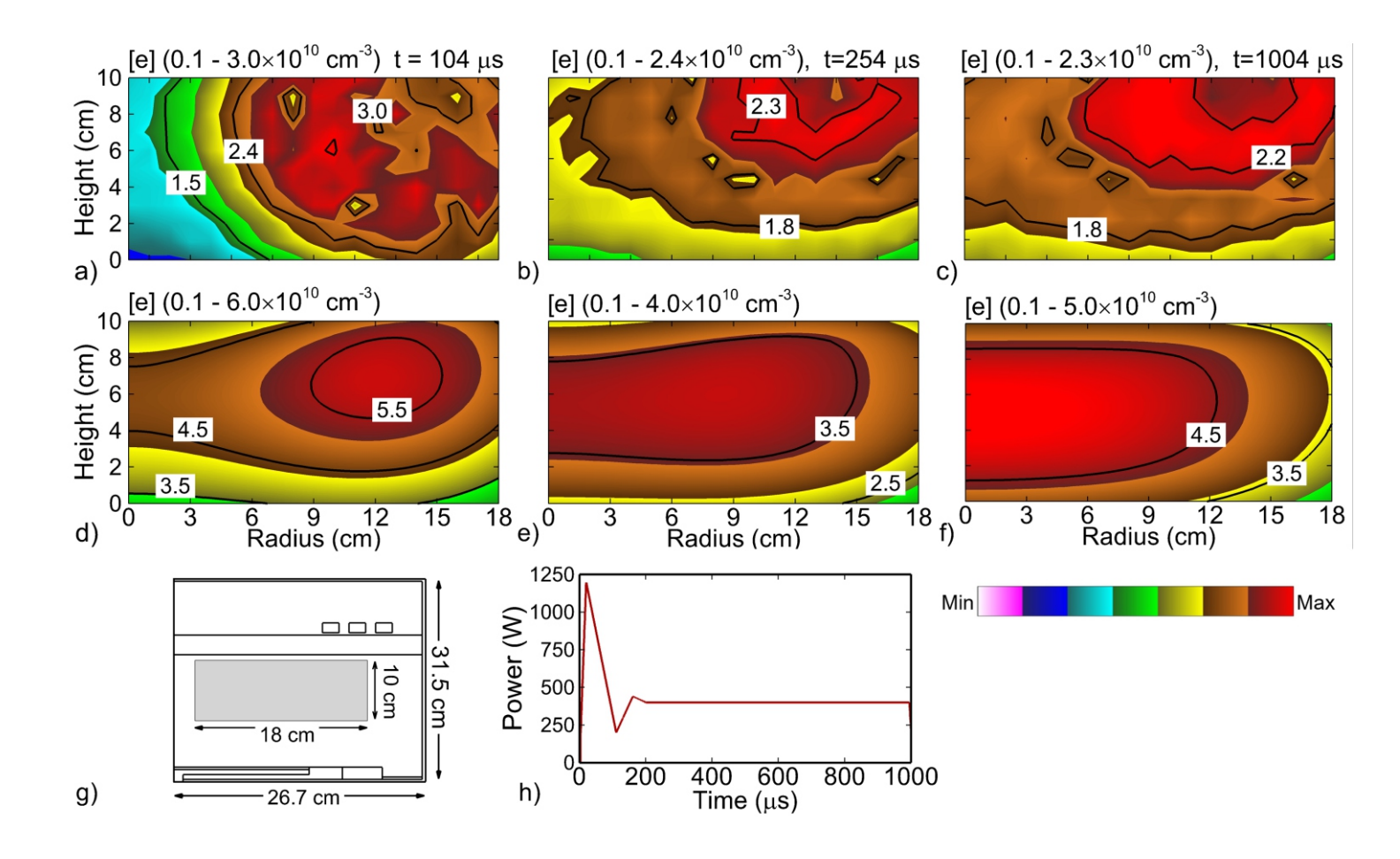
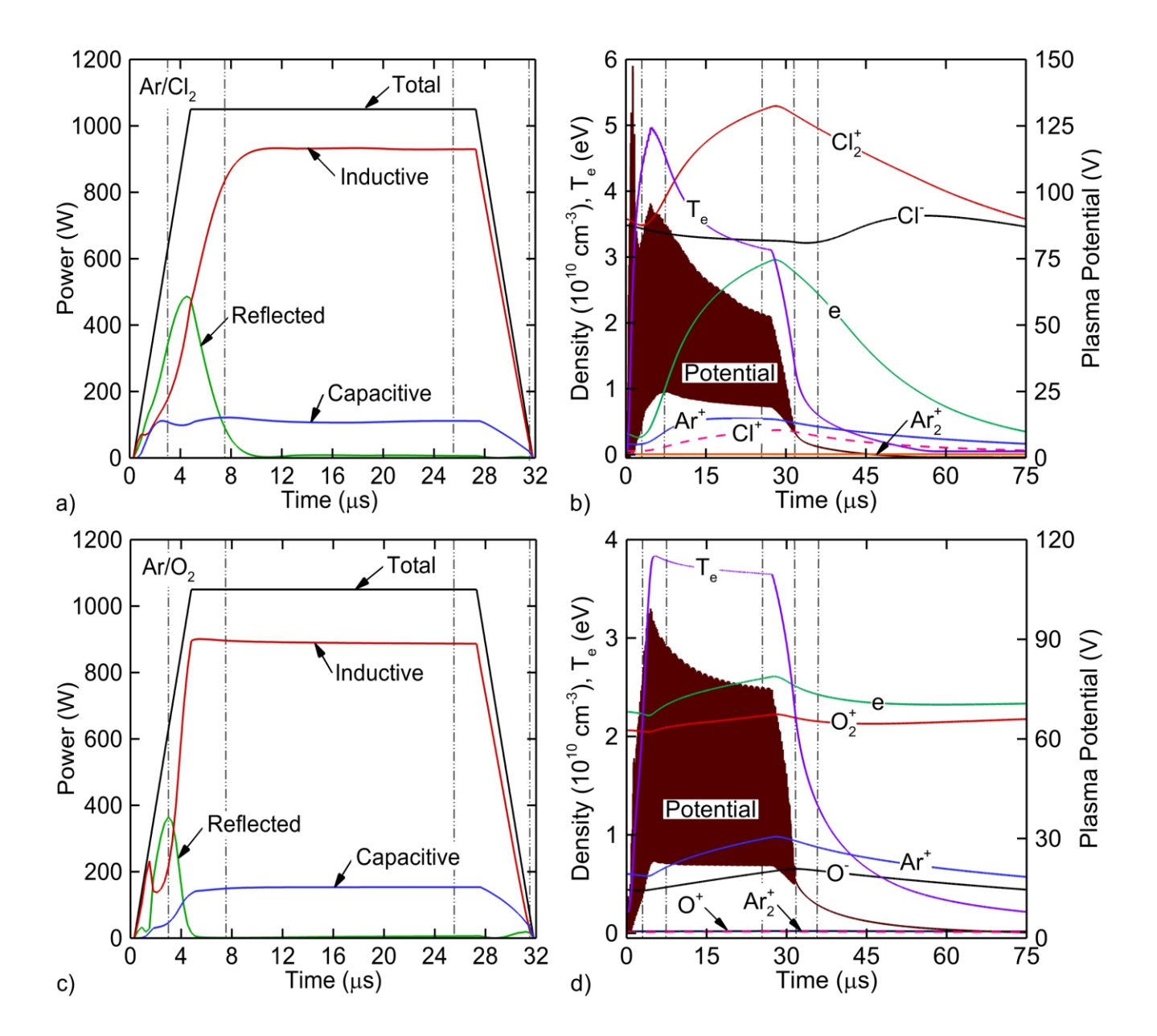
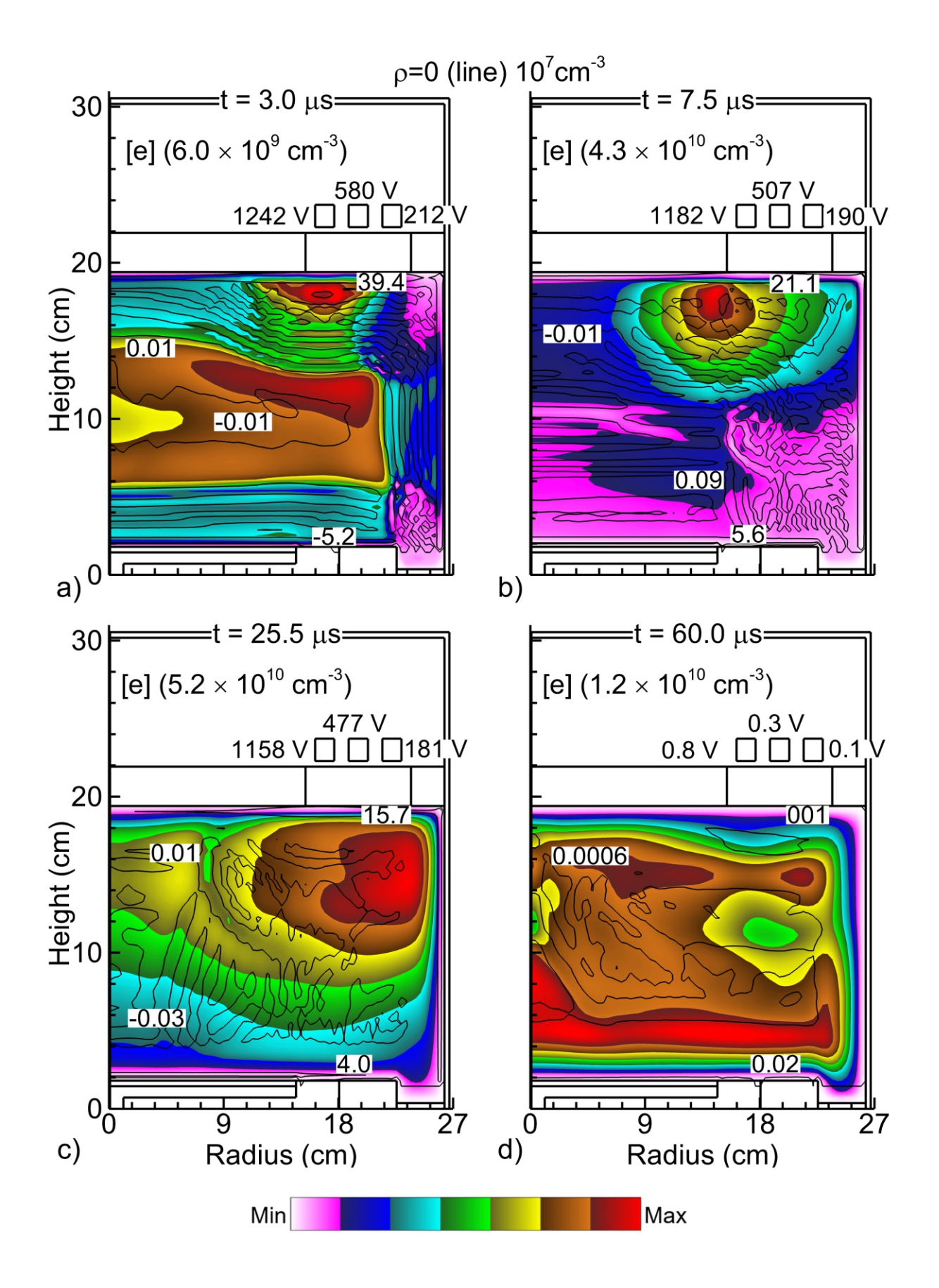


Figure 3 of 19







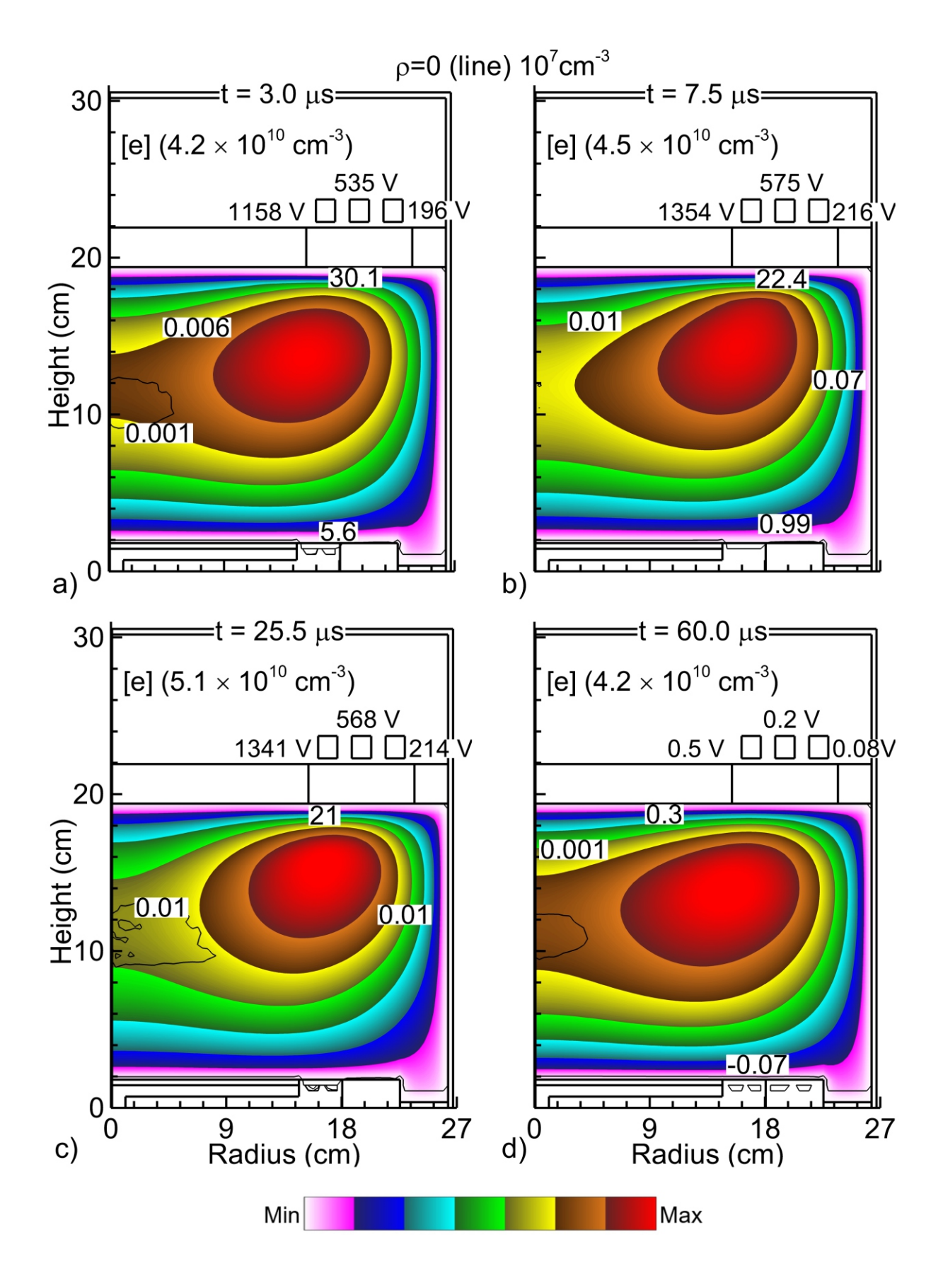
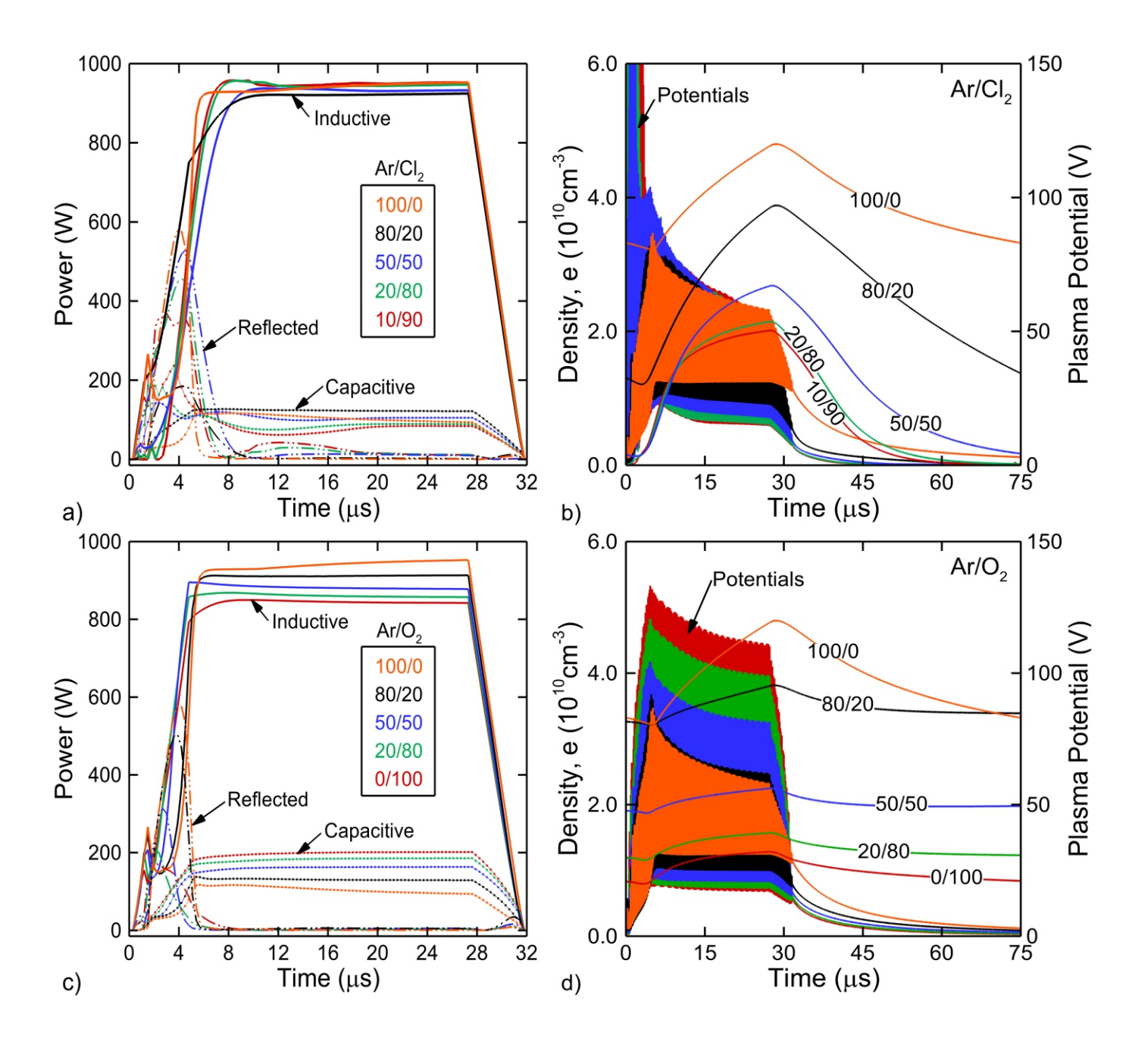


Figure 7 of 19



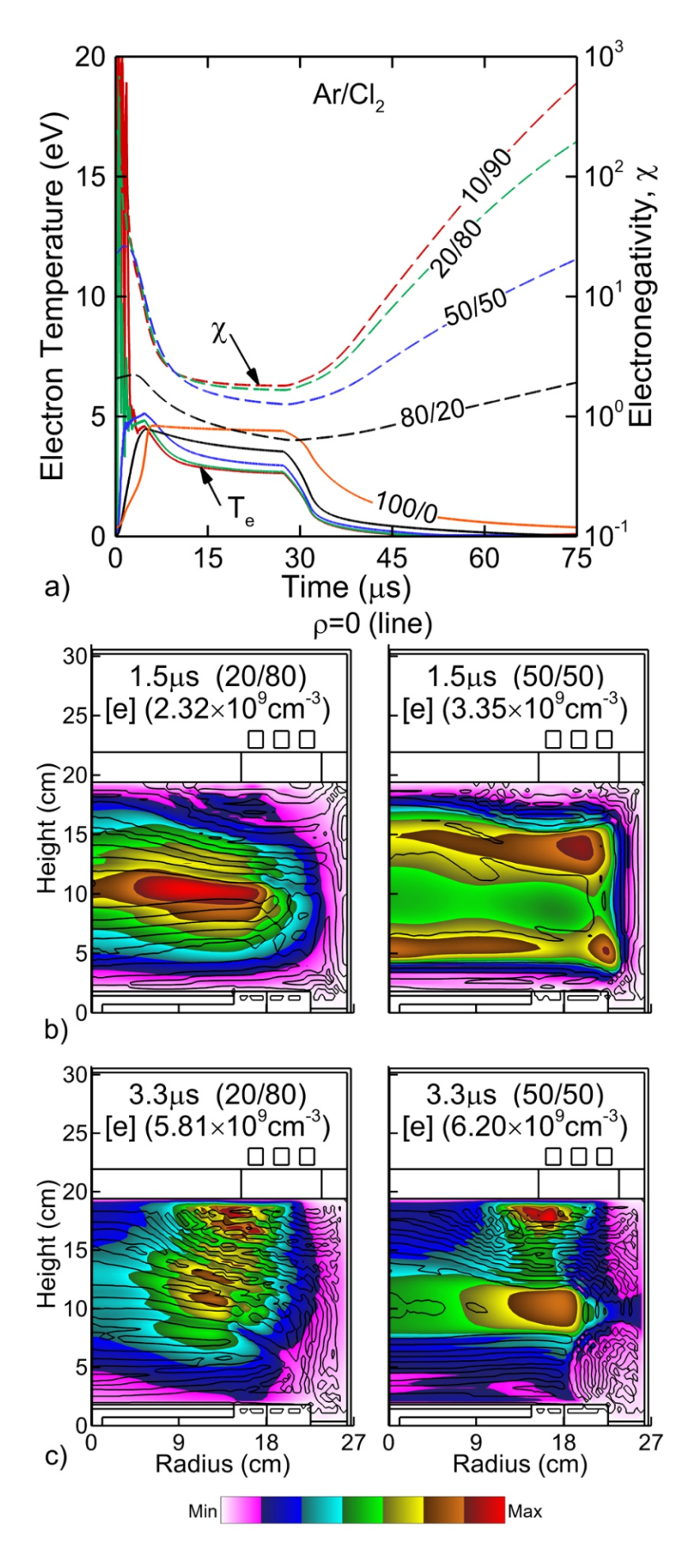
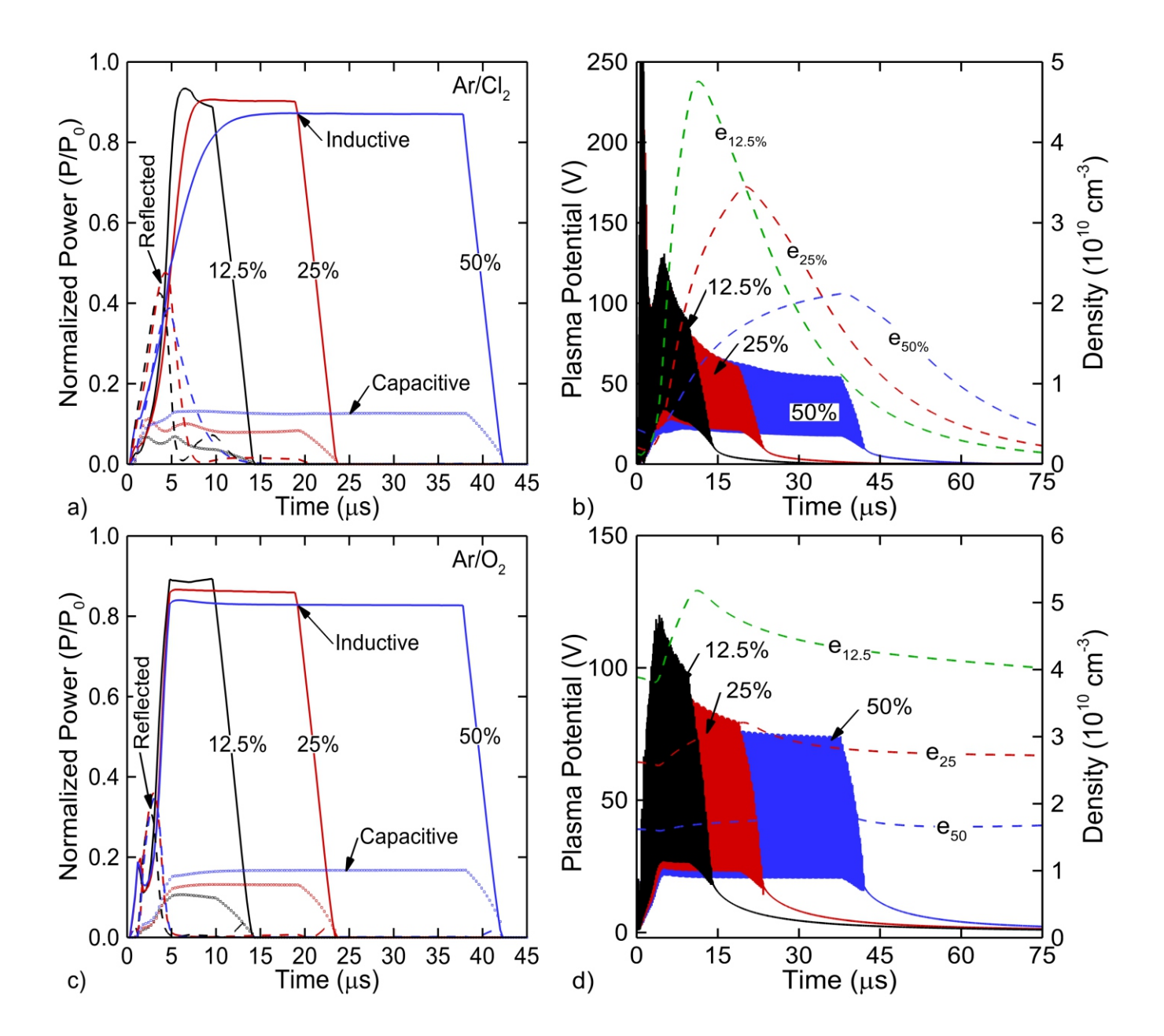
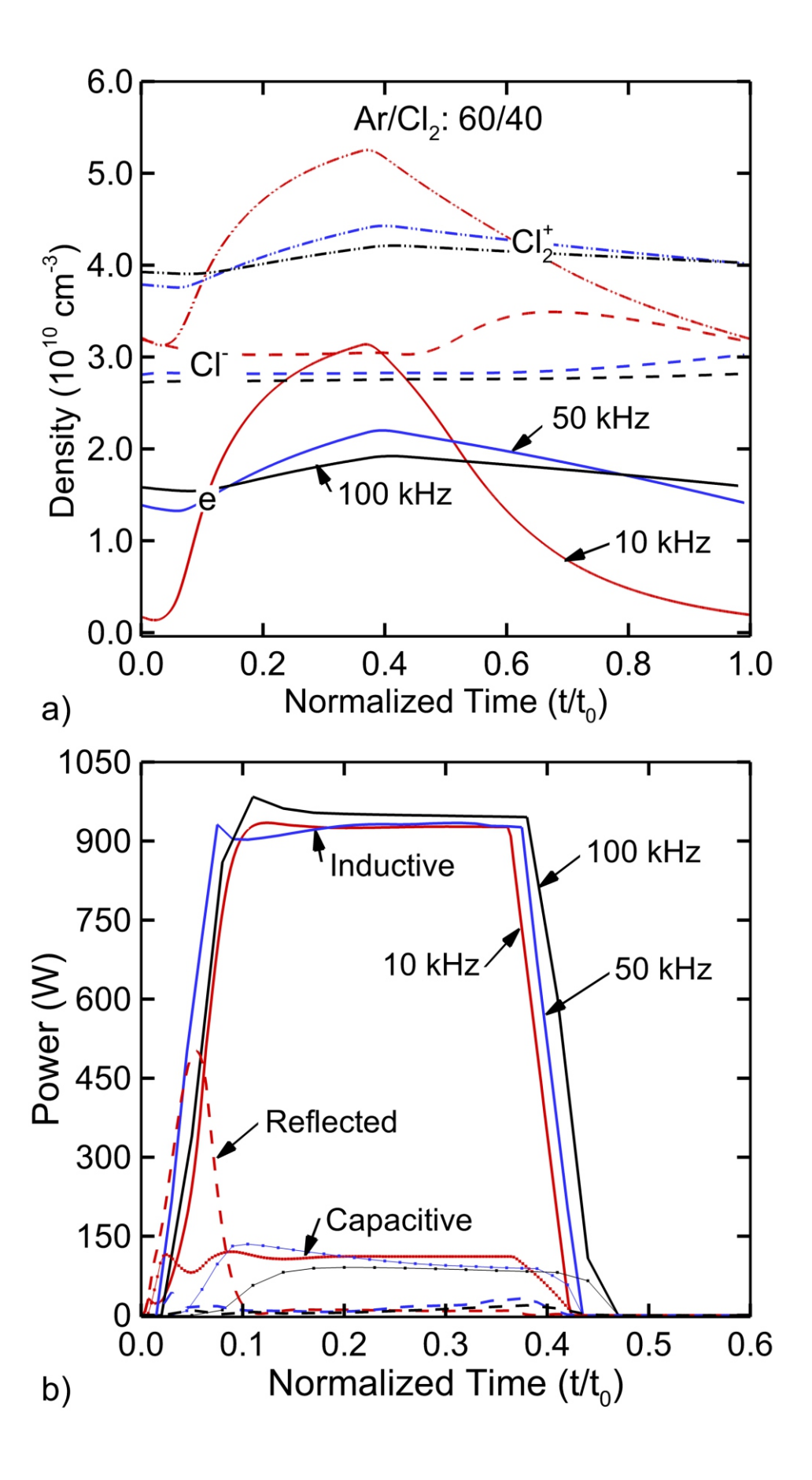
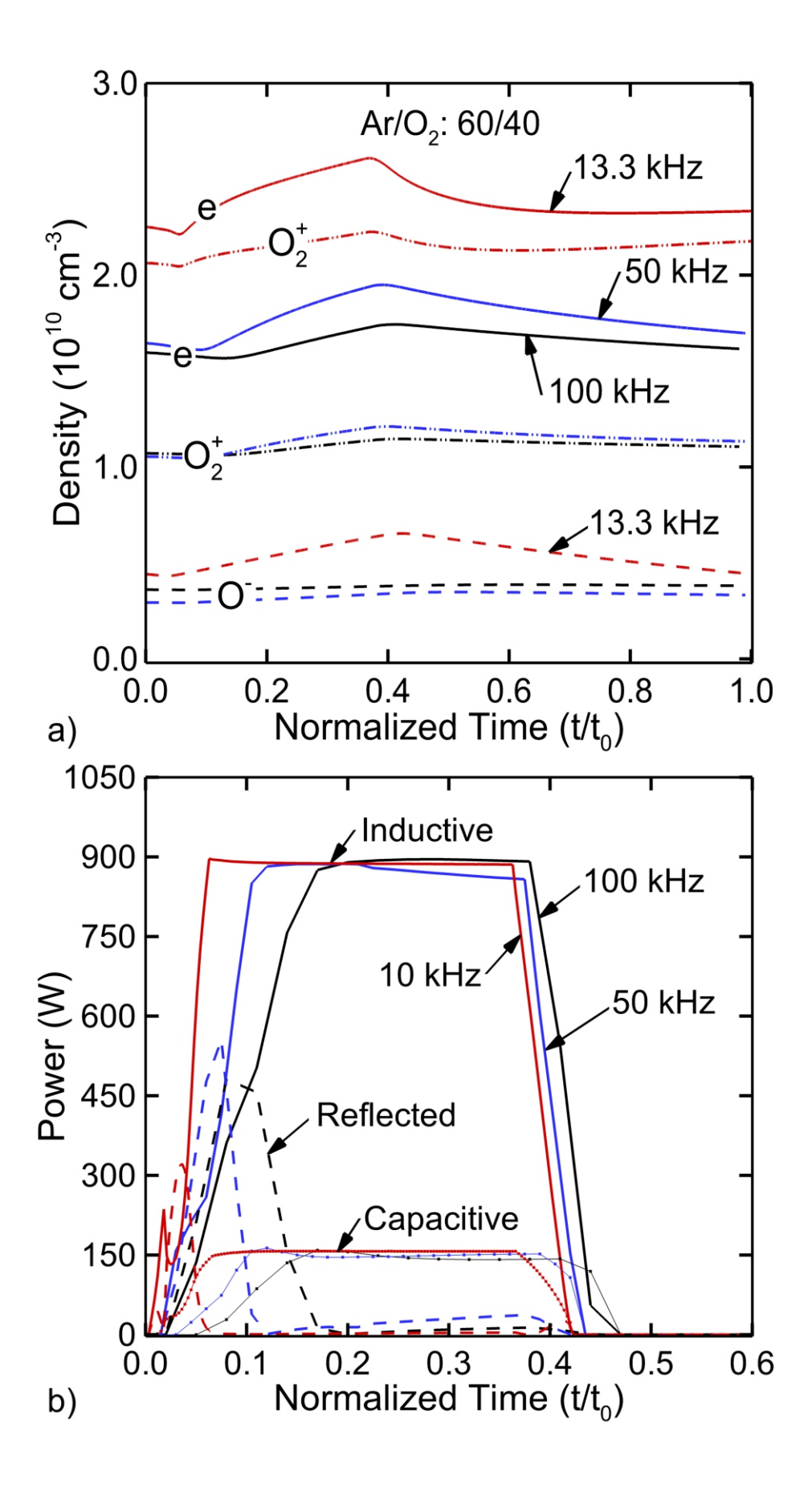


Figure 9 of 19







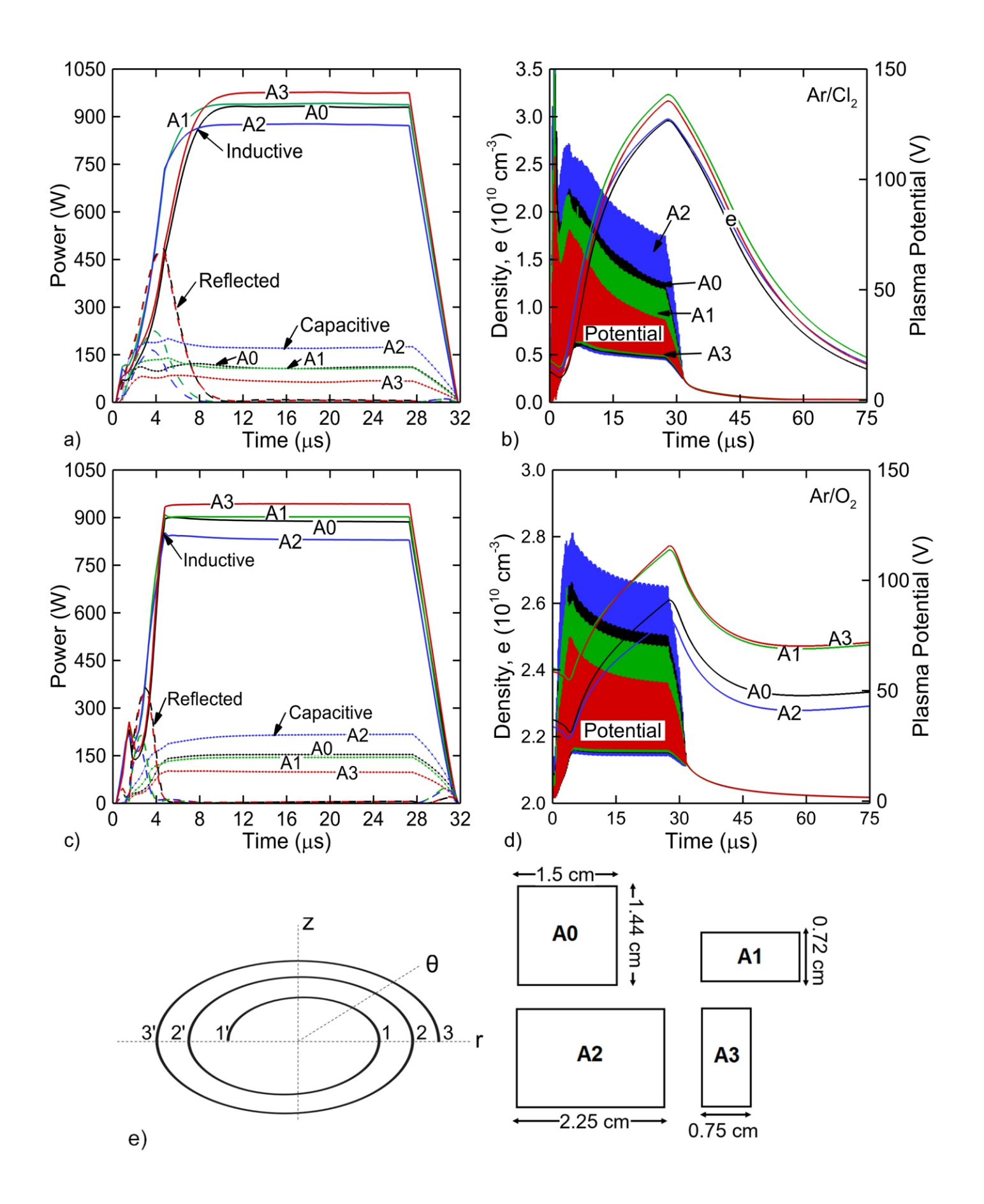
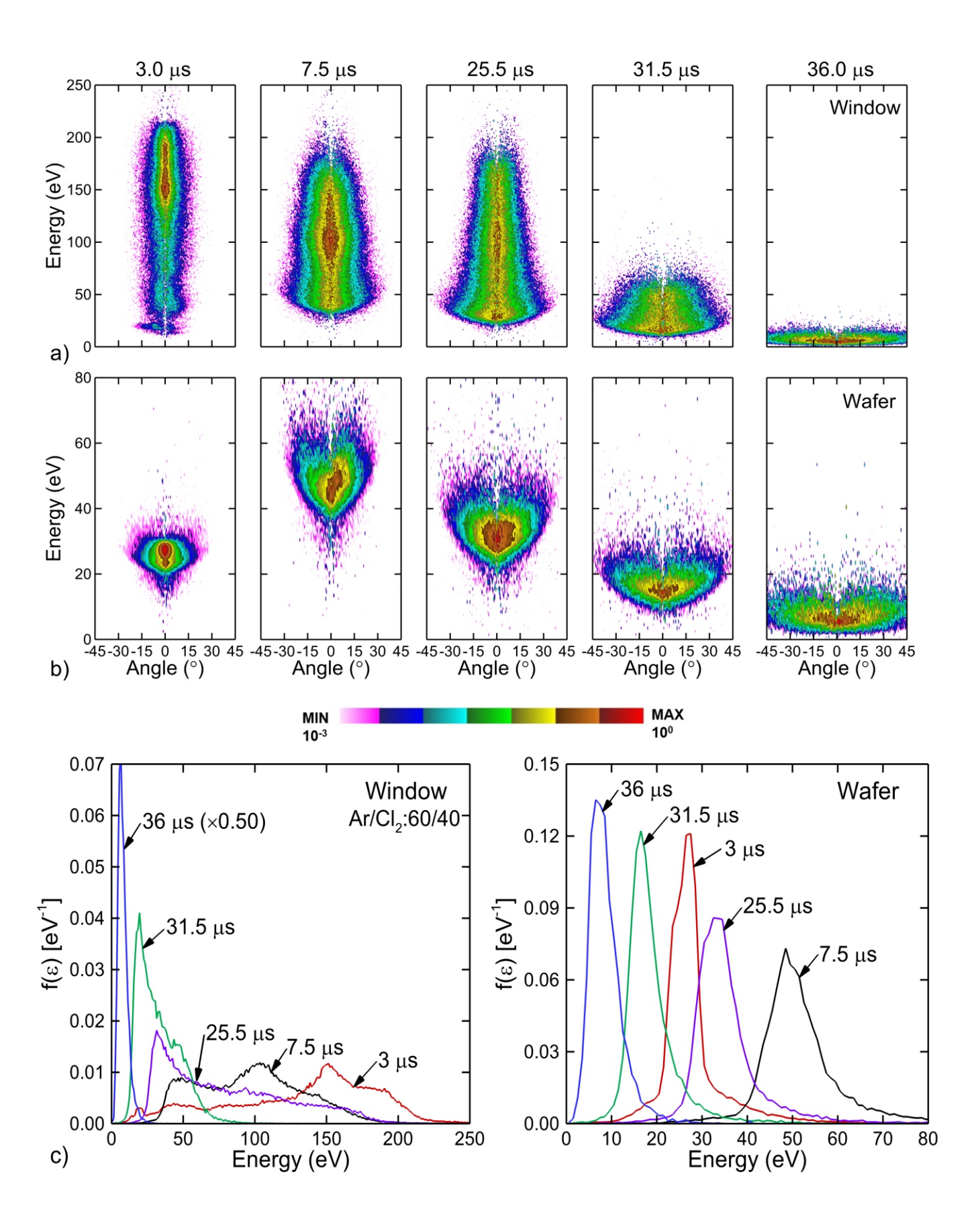
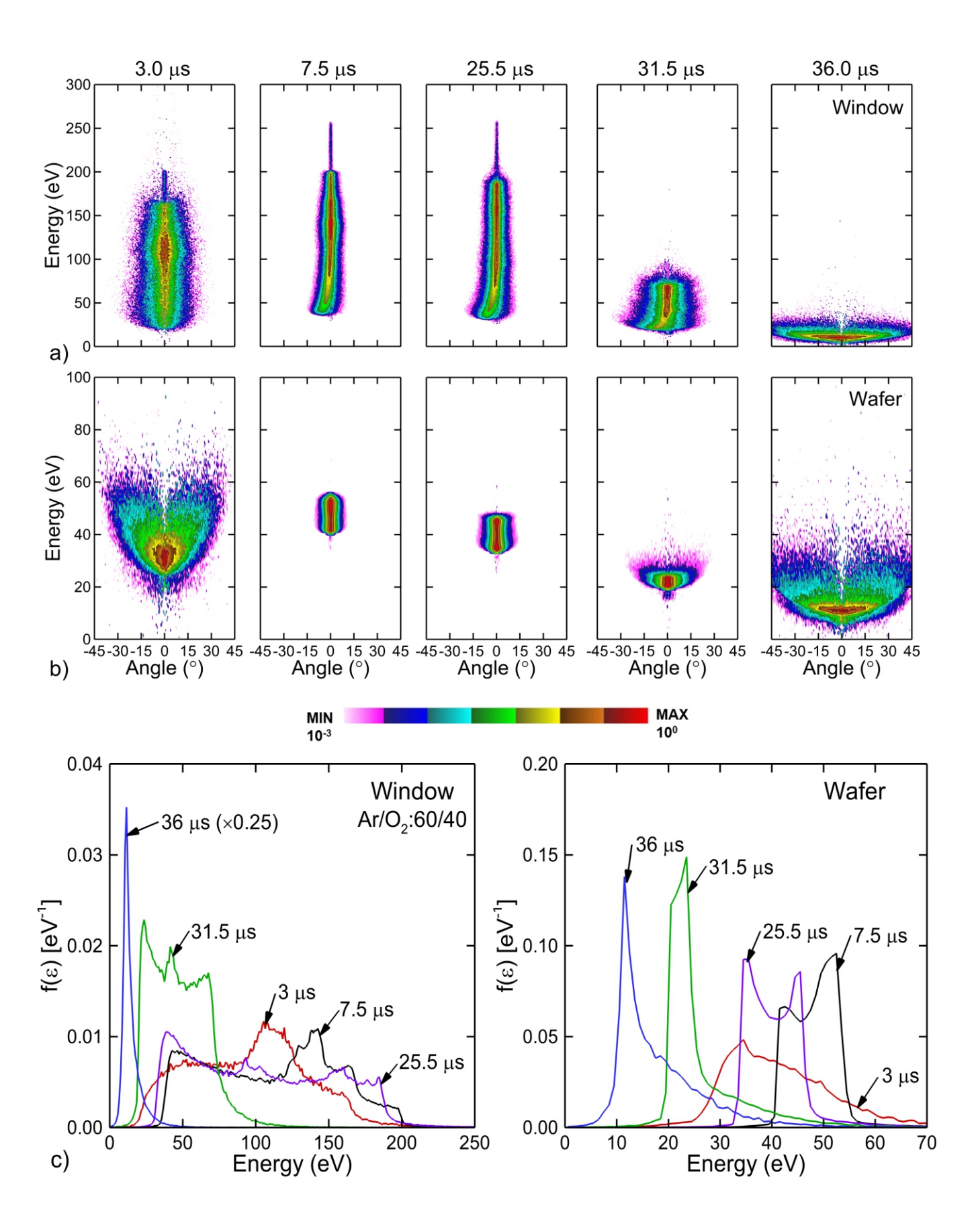
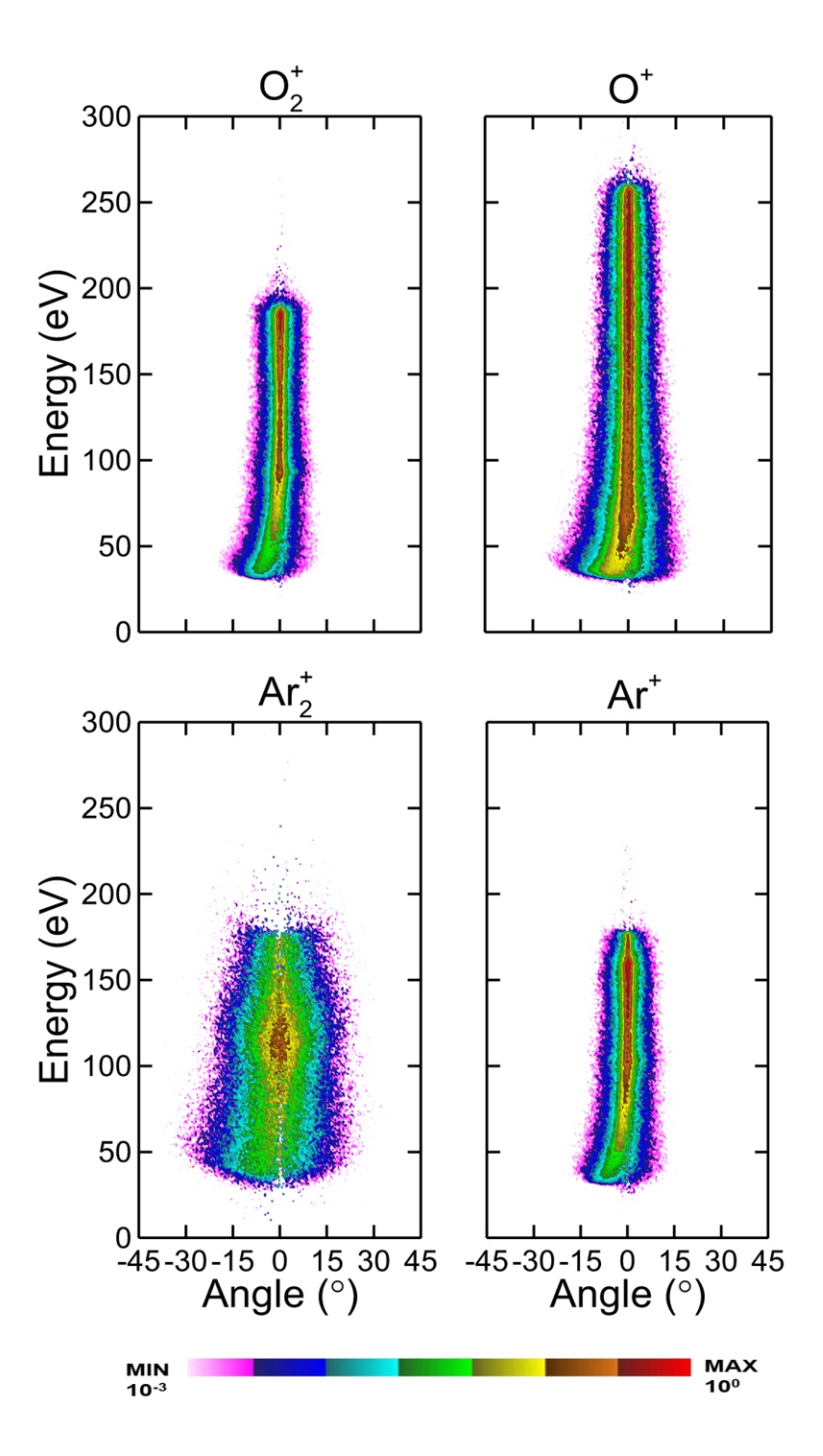
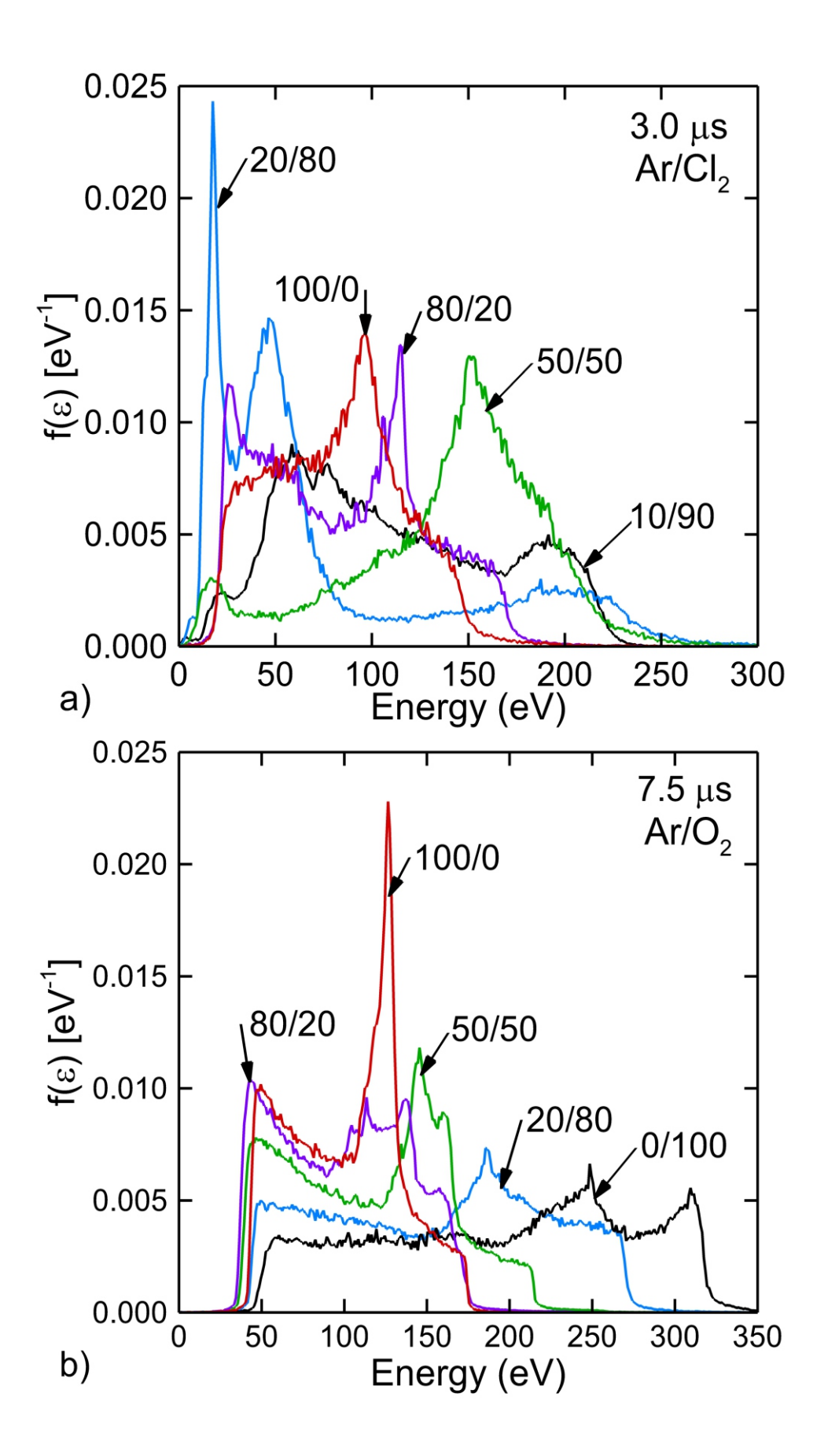


Figure 13 of 19









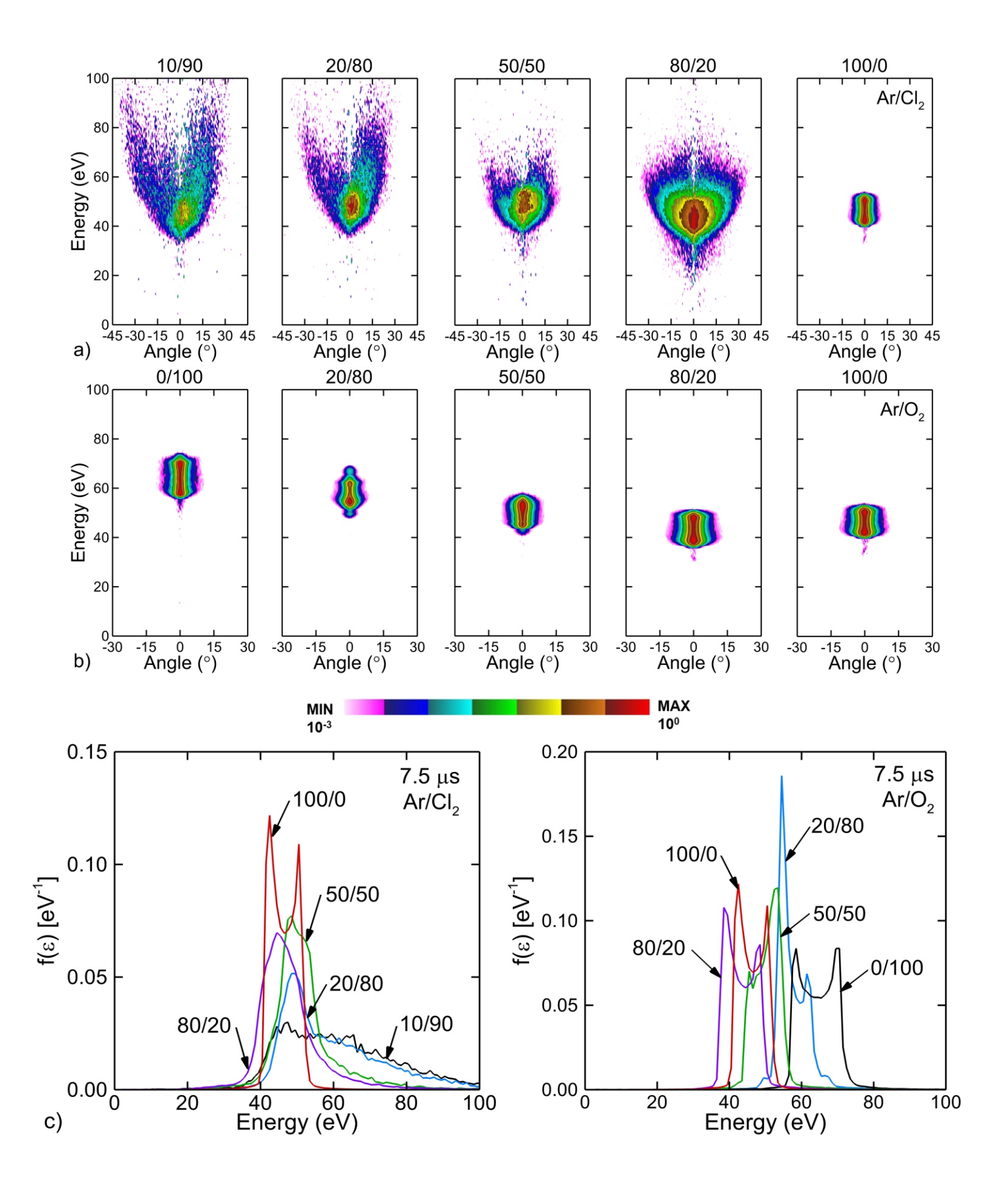


Figure 18 of 19

